Site-specific analysis reveals candidate cross-kingdom small RNAs, tRNA and rRNA fragments, and signs of fungal RNA phasing in the barlsupplementary fileey-powdery mildew interaction

Running title: Site-specific enrichment of host/pathogen small RNAs

Stefan Kusch[1], Mansi Singh[1], Hannah Thieron[1], Pietro D. Spanu[1,2,*], Ralph Panstruga[1]

[1] Unit of Plant Molecular Cell Biology, Institute for Biology I, RWTH Aachen University, Worringerweg 1, D-52056 Aachen, Germany

[2] Imperial College, London, United Kingdom

* **Corresponding author:**
Pietro Spanu, +44 207 5945384, p.spanu@imperial.ac.uk

Abstract

The establishment of host-microbe interactions requires molecular communication between both partners, which involves the mutual transfer of noncoding small RNAs. Previous evidence suggests that this is also true for the barley powdery mildew disease, which is caused by the fungal pathogen *Blumeria hordei*. However, previous studies lacked spatial resolution regarding the accumulation of small RNAs upon host infection by *B. hordei*. Here, we analysed site-specific small RNA repertoires in the context of the barley-*B. hordei* interaction. To this end, we dissected infected leaves into separate fractions representing different sites that are key to the pathogenic process: epiphytic fungal mycelium, infected plant epidermis, isolated haustoria, a vesicle-enriched fraction from infected epidermis, and extracellular vesicles. Unexpectedly, we discovered enrichment of specific 31- to 33-base long 5'-terminal fragments of barley 5.8S ribosomal RNA (rRNA) in extracellular vesicles and infected epidermis, as well as particular *B. hordei* tRNA fragments in haustoria. We describe canonical small RNAs from both the plant host and the fungal pathogen that may confer cross-kingdom RNA interference activity. Interestingly, we found first evidence of phased small RNAs (phasiRNAs) in *B. hordei*, a feature usually attributed to plants, which may be associated with the post-transcriptional control of fungal coding genes, pseudogenes, and transposable elements. Our data suggests a key and possibly site-specific role for cross-kingdom RNA interference and noncoding RNA fragments in the host-pathogen communication between *B. hordei* and its host barley.

Keywords

RNA interference, powdery mildew, barley, *Blumeria*, haustorium, mycelium, extracellular vesicles, cross-kingdom RNAi, tRNA fragments, rRNA fragments, phased RNA, small RNA

Abbreviations

Ago	Argonaute
Dcl	Dicer-like
EPI	epidermis (colonized by *B. hordei* but epiphytic fungal mycelium removed)
dsRNA	double-stranded RNA
EV	extracellular vesicle
FDR	false discovery rate
GO	gene ontology
HAU	haustoria of *B. hordei*
milRNA	micro RNA-like
miRNA	micro RNA
MYC	mycelium of *B. hordei*
phasiRNA	phased siRNA

P40	microsomes from *B. hordei*-infected epidermis
RNAi	RNA interference
rDNA	ribosomal DNA
rRF	ribosomal RNA-derived small RNA fragment
rRNA	ribosomal RNA
sRNA	small RNA
siRNA	small interfering RNA
tasiRNA	trans-acting short interfering RNA
TPM	transcripts per million
tRF	transfer RNA-derived small RNA fragment
tRNA	transfer RNA

Introduction

All complex multicellular organisms, including plants, require the exchange of information between cells for development and reproduction, but also need to communicate signals between each other and to coordinate the response to external stimuli. This exchange is referred to as either intra- or inter-organismal communication, depending on whether it takes place between cells of the same organism or between separate organisms. A special case of inter-organismal communication is the exchange of information between organisms of different taxa. Examples of this phenomenon in the area of plant-microbe interactions comprise mutually advantageous symbioses and diseases caused by pathogenic fungi (1, 2). Gene regulation by non-coding small RNAs (sRNAs) can play an important role in the context of such plant-microbe encounters (1).

In plants, sRNAs are important for regulating and fine-tuning diverse processes including growth and development, maintenance of genome integrity, epigenetic inheritance, and facilitating responses to both abiotic and biotic stress (3, 4). Based on their biogenesis and function, sRNAs can be divided into two major subclasses, micro RNAs (miRNAs) and small-interfering RNAs (siRNAs, (5)). *Micro RNA* (*MIR*) genes encode pri-miRNAs, which are further processed into pre-miRNAs and finally mature miRNAs. In eukaryotes other than mammals and plants, such as in fungi, it is challenging to prove the presence of *bona fide* miRNAs due to lack of evidence for the non-functional miRNA precursor strand; for this reason, they are termed miRNA-like RNAs (milRNAs; (6)). In contrast to miRNAs, siRNAs are generated from double-stranded DNA molecules of various origins (5). In some cases, miRNAs trigger the generation of secondary siRNAs, for example phased siRNAs (phasiRNAs; i.e., regularly spaced siRNAs that derive from a common precursor RNA), which are sometimes associated with the silencing of transposable elements (7). If the sRNA that triggers the formation of phasiRNAs is derived from a remote *trans*-acting sRNA locus, it is termed *trans*-acting siRNA (tasiRNA; (7)). While phasiRNAs and tasiRNAs are well-described in plants, they are largely unexplored in fungi, as we are aware of only one study reporting their existence in the fungal kingdom (8).

Both classes of sRNAs can induce either transcriptional gene silencing or posttranscriptional gene silencing of specific target genes, collectively referred to as RNA interference (RNAi; (9)). Irrespective of the class, biogenesis and function of the sRNA, RNAi involves cleavage of a double-stranded RNA (dsRNA) molecule by a dicer-like (Dcl) ribonuclease and loading of the mature sRNA onto an Argonaute (Ago) protein, together forming the RNA-induced silencing complex (5). Dcl proteins process the dsRNA precursor fragments into smaller pieces of 21-24 nucleotides or bases. The length of the fragment produced depends on the specific Dcl proteins, which recognise different types of dsRNA. The fragments are then bound by Ago proteins that specifically distinguish different sRNA lengths and are associated with distinct modes of gene silencing. For example, *Arabidopsis thaliana* AGO1 binds 21 base-long miRNAs generated by DCL1 or DCL4 and executes posttranscriptional gene silencing by cleaving target mRNAs in a sequence-specific manner. By contrast, *A. thaliana* AGO4 binds almost exclusively 24 base-long siRNAs generated by DCL3. AGO4 then induces transcriptional gene silencing by triggering DNA methylation, a process referred to as RNA-dependent DNA methylation (10). In each case, the Ago-bound sRNA determines target

116 specificity through sequence complementarity and the Ago protein is the key effector for
117 gene silencing. In the context of inter-organismal communication, the phenomenon of
118 sRNA-triggered trans-species gene silencing has been termed cross-kingdom RNAi. One of
119 the best studied systems for plant-microbe cross-kingdom RNAi is the *A. thaliana-Botrytis*
120 *cinerea* pathosystem, where exchange of sRNAs occurs in both directions (11, 12). Once
121 fungal sRNAs reach plant cells they are loaded onto *A. thaliana* Ago proteins, which carry
122 out the cleavage of host target transcripts such as those encoding mitogen-activated protein
123 kinases (11). Similarly, the most abundant *A. thaliana* sRNAs detected in *B. cinerea* cells
124 originate from tasiRNAs or intergenic loci, and target fungal genes important for
125 pathogenicity (13).
126 Extracellular vesicles (EVs) may serve as shuttles for inter- and intraorganismal RNA
127 molecule transfer in the context of plant-microbe interactions (13). The release of EVs and
128 their contents into the plant apoplast upon pathogen challenge and their delivery to
129 infection sites was first described over 50 years ago (14, 15). This parallels the situation in
130 mammalian cells where EVs in the intercellular space target nearby and distant cells and are
131 important components of intra-organismal communication (16). The EVs interact with
132 recipient cells to deliver cargo like sRNAs by membrane fusion and vesicle internalisation
133 (17–19). EVs occur in all pro- and eukaryotic phyla (20). However, it is still unclear whether
134 EV shuttling is the main mechanism for the delivery of sRNAs in plant-pathogen interactions,
135 since evidence for the shuttling of sRNAs outside of EVs was recently found in *A. thaliana*
136 (21).
137 The agronomically important crop barley (*Hordeum vulgare*) is the host plant of the
138 ascomycete fungus *Blumeria hordei*, previously named *B. graminis* f.sp. *hordei* (22), which
139 causes the powdery mildew disease on barley. *B. hordei* colonises barley biotrophically and
140 the obligate relationship between host and pathogen requires tightly controlled gene
141 regulation. In a previous study, we found that the essential components of the RNAi
142 machinery are present in *B. hordei* (23). Moreover, we discovered at least 1,250 sRNA loci in
143 the *B. hordei* genome, of which 524 were predicted to have mRNA targets in the host barley.
144 Expression of sRNAs in both barley and *B. hordei* is consistent with a role in regulating
145 transcript abundance in both partners during the interaction (24). In *B. hordei*, milRNAs may
146 control the mRNA levels of fungal virulence genes whereas barley miRNAs and phasiRNAs
147 might control transcript levels of components of the plant innate immune system. Inter-
148 organismal exchange of RNAs is thought to be mediated by membrane-bound vesicles (13).
149 Interestingly, vesicle-like structures have been observed at the interface between *B. hordei*
150 infection structures and barley leaf epidermal cells (25, 26); this finding would be consistent
151 with an exchange of sRNAs mediated by EVs in the context of the barley-powdery mildew
152 interaction.
153 In this study, we analysed the sRNA spectrum in the *B. hordei* - barley pathosystem. To this
154 end, we dissected infected leaves into separate fractions representing different sites that
155 are key to the pathogenic process, i.e., epiphytic fungal mycelium, infected plant epidermis,
156 isolated haustoria, a vesicle-enriched fraction from infected epidermis, and EVs.
157 Unexpectedly, we discovered enrichment of specific 31- to 33-base long 5' fragments of
158 barley 5.8S ribosomal RNA (rRNA) in EVs, vesicles, and infected epidermis, as well as specific
159 *B. hordei* tRNA fragments in haustoria. We describe canonical sRNAs from both the plant

host and the fungal pathogen that may confer cross-kingdom RNAi activity. Interestingly, we found first evidence of phasiRNAs in *B. hordei*, a feature usually attributed to plants, which may be associated with the post-transcriptional control of coding genes, pseudogenes, and transposable elements. Our data suggests a key role for cross-kingdom RNAi and noncoding RNA fragments in the host-pathogen communication between *B. hordei* and its host barley.

Results

Site-specific sRNA sampling

Based on three independent experiments, we isolated total RNA from the following biological materials ("sites") of *B. hordei*-infected barley leaves four days after inoculation (Figure 1, see Materials and Methods for a detailed description of the samples): (1) Epiphytic fungal mycelium (MYC), (2) infected epidermis without mycelium (EPI), (3) fungal haustoria (HAU), (4) microsomes of the epidermis without mycelium (P40). In addition, RNA from (5) apoplastic extracellular vesicles (EV+) were isolated from *B. hordei*-infected barley leaves three days after inoculation. As a control, we also isolated (6) total RNA from extracellular vesicles of non-infected plants (EV-). The 18 RNA samples (6 sources, 3 replicates each) were then used to extract RNA, which was subsequently subjected to Illumina-based short read sequencing at a depth of 30 million (MYC, EPI, HAU, P40) or 20 million (EV+, EV-) reads per sample (Supplementary Table 1).

Distinct rRNA- and tRNA-derived sRNAs are enriched in *B. hordei*- and barley-derived sample materials

The length of the trimmed sRNA reads ranged from 15 to 75 bases. However, the majority of the reads were between 15 and 40 bases long; between 282,734 (2.4%) and 5,432,088 (13.8%) per sample cumulatively accounted for reads between 41-74 bases (Supplementary Table 2). We determined the sRNA length distribution profiles from the 15 to 40 base reads of the various samples and found that each of the six biological materials showed a distinctive and largely reproducible pattern: the sRNAs from mycelium (MYC) exhibited a bimodal distribution with a prominent peak at 21 and 22 bases, and a much shallower and broader peak with a maximum at 29-33 bases. Likewise, the epidermal (EPI) samples had a bimodal size distribution with marked peaks at 21-22 and 32-33 bases, respectively. The HAU and P40 samples exhibited a broad size range without any outstanding peak, but an increase in the number of 27-32 bases reads compared to reads below or above this range. Finally, the two EV sample types (EV- and EV+) exhibited distinctive profiles: the EV+ size distribution was reminiscent of EPI and MYC samples, with a bimodal distribution and characteristic peaks at 21-23 and 31-32 bases, respectively. However, the EV- sRNAs showed a single prominent peak at 31-32 bases (Supplementary Figure 1A).

We mapped the sRNA reads to the respective reference genomes of *H. vulgare* IBSCv2 (27) and *B. hordei* DH14 (28) using bowtie within the ShortStack (29) pipeline. Overall, between 3,715,684 and 32,777,442 reads could be assigned to the *H. vulgare* genome and between 431,626 and 22,069,070 reads to the *B. hordei* genome, respectively (Supplementary Table

204 1). We next determined the number of reads mapping to each of the genomes separately
205 for the read sizes of 15-40 bases (Supplementary Figure 1B; Supplementary Table 3 and 4).
206 We noted that reads below 19 bases could not be unequivocally allocated to either
207 organism by read mapping alone, resulting in >100% total mapping counts. Hence, we
208 considered reads <19 bases as ambiguous and disregarded these from further read length-
209 related analysis. We found that the majority of 21-22 base reads in the MYC and EPI samples
210 derived from the *B. hordei* genome, while reads from the 31-32/32-33 base peaks in the EPI
211 and EV samples almost exclusively aligned to the genome of *H. vulgare*. The majority of
212 reads >19 bases from the P40 and EV- samples were from the *H. vulgare* genome, while
213 reads from the EPI, HAU, and EV+ samples originated from both organisms. Regardless of
214 the read length, except for the distinct 31/32/33 base peak in reads from *H. vulgare*, the
215 majority of the reads originated from either coding genes or transposable elements
216 (Supplementary Figure 2).
217 We next explored the identity and possible molecular origin of the sRNAs from the very
218 prominent 31-32 base peak in the EV+ and 32-33 base peak in the EPI samples, both from
219 *B. hordei*-infected barley leaves. Using MMSeqs2 for BLAST against the RNA families (RFAM)
220 databases of conserved noncoding RNAs (i.e., transfer RNAs, ribosomal RNAs, small
221 nucleolar RNAs, small nuclear RNAs), we found that >80% of the sequences in these two
222 sample types corresponded to a specific short fragment of the barley 5.8S rRNA (Figure 2).
223 This 5.8S rRNA fragment (rRF) was specifically found in 31-32-base long reads in EV+ and EV-
224 , and 32-33-base long reads in EPI (Supplementary Figure 3). In case of the EV- sample,
225 approximately 30% of 31-32 base reads match this barley 5.8S rRF, while only <15% of P40
226 and HAU reads originate from it. Between 15 and 30% of the reads in the MYC and HAU
227 samples were identified as derived from *B. hordei* 5.8S rRNA (Figure 2). In HAU, *B. hordei*
228 5.8S rRNA fragments were abundant in reads of 27-32 bases in length (Supplementary
229 Figure 3). Notably, the vast majority of the 5.8S rRNA-associated reads mapped to the 3'-
230 end of the molecule in both organisms, even in samples lacking a distinctive peak at 31-33
231 bases (>90%; Figure 2B and Table 1). We refer to these regions as *H. vulgare* rRNA fragment
232 *Hvu*-rRF0001 and *B. hordei* rRNA fragment *Bho*-rRF0001 (Figure 2B and Table 2). In case of
233 *B. hordei*, we found a second less abundant fragment adjacent to *Bho*-rRF0001, called
234 *Bho*-rRF0002 (Supplementary Figure 3 and Table 2).
235 In the P40 and HAU samples, which had a broad peak from 27 to 32 bases (Supplementary
236 Figure 1), a large portion of reads was identified as 28S (large subunit, LSU) rRNA-derived
237 sRNAs (Figure 2 and Supplementary Figure 3). P40 had >60% of barley 28S rRNA-originating
238 reads, while HAU reads could be mapped to >25% barley and >20% *B. hordei* 28S rRNA
239 sequences. We aligned these reads in a targeted manner to the 28S LSU rRNAs of *H. vulgare*
240 and *B. hordei* and noted distinct prominent peaks, suggesting the enrichment of specific 28S
241 rRFs in *B. hordei*-infected barley plants (Supplementary Figure 4 and 5, Supplementary Table
242 5 and 6). In case of the barley 28S rRNA, the first peak was approximately at position 2,100-
243 2,150 (*Hvu*-rRF0002) and the second peak around position 3,760-3,800 (*Hvu*-rRF0003); both
244 peaks were distinctive in the HAU and P40 samples. The peak corresponding to *Hvu*-rRF0002
245 was shifted to 2,230-2,270 in EV+ samples (*Hvu*-rRF0004), while the peak at 2,100-2,150 was
246 somewhat split and shifted to positions 2,340-2,380 in the EV- sample (*Hvu*-rRF0005). For
247 *B. hordei*, the 28S rRNA-derived sRNAs mapped to a peak at position 430-470 (*Bho*-

248 rRF0003), which is distinctive in the EPI, HAU, and MYC samples. In addition, a second peak
249 at position 1,620-1,660 (*Bho*-rRF0004) appeared in the samples HAU and P40. Notably, we
250 detected a peak at position 2,150-2,180 in the EV+ sample, which is probably due to the
251 high identity between the two 28S rDNA sequences between *H. vulgare* and *B. hordei* in this
252 position (Supplementary Figure 5D).
253 More than 60% (3,557,695) of the reads from the MYC sample were identified as *B. hordei*
254 tRNA-derived sRNAs (tRNA fragments (tRFs); Figure 2). Intriguingly, >48% of these appear to
255 originate from *B. hordei* tRNAs with anticodons for glutamine (Gln) (Figure 2D). The 5'
256 moiety of the UUG anticodon Gln tRNA accounted for 1,332,676 reads (37%), 424,142 reads
257 (11.9%) were from the 5' end and 124,372 (3.5%) from the 3' end of the CUG anticodon Gln
258 tRNA, and 314,017 reads (8.8%) were identified as the 3' moiety of the UUC anticodon Glu
259 tRNA. Next, we predicted the putative secondary structures and minimum free energy of
260 the rRNA and tRNA fragments using the Vienna RNAfold webserver (30) to assess if they
261 would be thermodynamically stable (Supplementary Table 7). Notably, *Hvu*-rRF0001 was
262 predicted to form a secondary structure that was particularly stable, forming two double-
263 stranded helices at a free energy of -11.9 kcal mol^{-1} (Supplementary Figure 6). This was
264 markedly more stable than any other theoretical fragment that could be derived from the
265 barley rRNA (between -1.5 and -4.7 kcal mol^{-1}) and also than the *B. hordei* 5.8S rRNA-derived
266 fragments (-5.3 and -3.4 kcal mol^{-1}, respectively). However, not all abundant rRNA
267 fragments exhibited low free energy (range between -2.4 and -11.9 kcal mol^{-1};
268 Supplementary Table 7). Similarly, the predicted secondary structures of the *B. hordei* tRNA
269 fragments ranged from -1.7 to -10.4 kcal mol^{-1} free energy, overall suggesting that the tRNA
270 and rRNA fragments we observed (Table 2) may assume secondary structures that are
271 thermodynamically stable, but calculated free energy is insufficient evidence to explain the
272 high abundance of most fragments in our dataset.
273 To assess if specific rRNA fragments occur frequently in infected plants, we then mined
274 publicly available sRNA sequencing datasets from barley, wheat (*Triticum aestivum*),
275 soybean (*Glycine max*), and *Arabidopsis thaliana* under various biotic and abiotic stresses
276 (see Supplementary Table 8 for all accessions). These data showed that read length
277 distributions varied between experiments even within the same species (Supplementary
278 Figure 7). Notably, we did not find striking rRNA enrichment in response to infection or
279 abiotic stress in this subset of sequencing data (Supplementary Figure 8). The fact that
280 another *B. hordei* sRNA-seq dataset (24) also lacks evidence for abundant rRNA suggests
281 that these fragments either appear late in infection (three to four days post inoculation in
282 our samples versus 48 hours post inoculation in (24)) or are only detectable in sampling
283 material enriched with infected host cells. Altogether we identified distinctive barley 5.8S,
284 28S (both barley and *B. hordei*), and *B. hordei* tRNA-derived sRNAs enriched in *B. hordei*-
285 infected barley samples (Table 2).
286
287 **Identification of microRNA-like (milRNA) genes in *B. hordei* and in barley**
288 Next, we used the ShortStack pipeline (Materials and Methods) to annotate and quantify
289 our sRNA samples. Because *bona fide* miRNAs are difficult to predict in fungi (6), we
290 identified microRNA-like RNAs (milRNAs) that satisfy all conditions of miRNAs except
291 detection of the precursor strand. Cumulatively, we identified 2,711 unique *B. hordei* and

292 35,835 unique barley milRNA loci with this pipeline, accounting for 2,558 and 29,987 unique
293 milRNA sequences, respectively (Supplementary Table 9; Supplementary Files 2-5). Of these,
294 three *B. hordei* milRNAs and 59 barley sequences were classified as *bona fide* miRNAs by
295 ShortStack. For *B. hordei*, most milRNAs were detected in the EPI, MYC, HAU, and EV+
296 samples (more than 200 milRNAs each), reflecting the abundance of fungal reads in these
297 samples. In case of *H. vulgare*, EPI and MYC samples represented the largest numbers of
298 milRNAs (more than 5,000 each), followed by the EV-, HAU, and P40 samples.
299 Then, we determined read counts for milRNA loci in both *H. vulgare* and *B. hordei* using the
300 read mapping information from ShortStack (Supplementary Table 10 and 11). We analysed
301 sample relatedness by using non-metric multi-dimensional scaling (NMDS), which collapses
302 multidimensional information into few dimensions (two in this case; Figure 3). In case of
303 *H. vulgare*, the three replicates of MYC, EPI, HAU, and P40 each formed distinct clusters,
304 while the EV+ samples were distinct but only broadly clustered, suggesting stronger
305 variation between replicates. EV- samples did not show clear clustering, as two data points
306 were similar to the EPI and MYC samples, and one was similar to the EV+ samples
307 (Figure 3A). The replicates distributed similarly in case of the *B. hordei* samples, but P40
308 samples showed a broader distribution and some overlap with the EV+ sample (Figure 3B).
309 For both *H. vulgare* and *B. hordei*, the samples showed comparable Pearson-based
310 hierarchical clustering (Figure 3C and 3D) and clustering trends in principal component
311 analysis (PCA; Supplementary Figure 9); ANOSIM testing confirmed significant sample
312 differentiation in both *H. vulgare* and *B. hordei* (p < 1e-4). EV- replicate three, which
313 clustered with EV+ samples, also showed the distinct peak of 31-32-base long reads,
314 enrichment of barley 5.8S rRNAs and *B. hordei* tRNAs, and of 28S rRNA-derived fragments
315 (Supplementary Figure 10). The 31-32-base peak was also visible in EV- replicate two and
316 consisted of >25% *B. hordei* 5.8S rRNA-derived and >50% tRNA-derived sRNAs. This suggests
317 that EV- replicates two and three represent vesicles from unintentionally infected rather
318 than non-infected barley leaves, and that the *H. vulgare* rRFs only occur due to infection
319 with *B. hordei* as the only replicate without apparent *B. hordei* sRNAs also lacks the peak at
320 31-32 bases. Together with the detection of *B. hordei* rRNA-derived reads of 31-33 bases in
321 length (Figure 2), these analyses suggest that at least one EV- sample was similar to the EV+
322 samples, another contained a significant number of *B. hordei*-derived sRNAs, and that EV
323 samples generally exhibited high variation hinting at a possible contamination of one or two
324 EV- samples and/or a low signal-to-noise ratio in the EV fractions.
325

326 **Site-specific accumulation of milRNAs**

327 We performed "weighted gene co-expression network analysis" (WGCNA) to identify
328 milRNAs associated with MYC, EPI, HAU, P40, and EV+ samples for 22,415 *H. vulgare* and
329 2,711 *B. hordei* milRNAs (Supplementary Figure 11), and then assigned 11,334 *H. vulgare*
330 and 2,325 *B. hordei* milRNAs as enriched in compartments with at least 2.5-fold abundance
331 above the average. 2,496 *H. vulgare* milRNAs were enriched in MYC, 1,137 in EPI, 422 in
332 HAU, 410 in P40, and 615 in EV+ (Figure 4A). In case of *B. hordei*, 519 milRNAs were
333 enriched in MYC, 260 in EPI, 108 in HAU, 59 in P40, and 26 in EV+ (Figure 4B). The samples
334 MYC and EPI also showed considerable overlap of equally abundant milRNAs, as 1,009 *B.*
335 *hordei* milRNAs and 3,628 *Hvu* milRNAs were more frequent in both samples. Further, 137

336 *B. hordei* milRNAs were associated with MYC, EPI, and HAU. We used psRNAtarget (31) to
337 predict RNAi targets of *H. vulgare* and *B. hordei* milRNAs. Overall, 3,693 *H. vulgare* milRNAs
338 had putative targets, i.e., 10,488 endogenous and 1,309 *B. hordei* unique transcripts (Figure
339 4). Ninety (6.8%) of the possible *B. hordei* target genes code for proteins with a predicted
340 secretion peptide. In case of *B. hordei* milRNAs, we found that 1,205 milRNAs could target
341 581 endogenous genes, 50 (8.6%) of which encode proteins with a predicted secretion
342 peptide, and 1,677 may target transcripts in the host *H. vulgare*. Notably, HAU-specific *B.*
343 *hordei* milRNAs had 76 potential cross-kingdom targets in *H. vulgare*, but only 23
344 endogenous targets. These milRNAs exhibited higher average abundance (837 transcripts
345 per million (TPM) on average) than, e.g., MYC-specific milRNAs (59 TPM average) or all
346 milRNAs (181 TPM average). The *B. hordei* milRNAs enriched in HAU and P40 (23 milRNAs,
347 5,768 TPM on average) exhibited a similar pattern, predicted to target altogether 12
348 *H. vulgare* genes and only one *B. hordei* gene.
349 We then performed global and subset-specific gene ontology (GO) enrichment analysis of
350 the putative cross-kingdom milRNA targets (Figure 5; Supplementary Table 12 and
351 Supplementary Table 13). We found significant GO enrichment in three of the *B. hordei*
352 milRNA cross-kingdom target sets (Figure 5A). Protein phosphorylation-related terms
353 (GO:0006468 and GO:0016773) were enriched between 3.6- and 12.9-fold in all three of the
354 milRNA cross-kingdom target sets ($P_{adj} < 0.05$). "ATP binding" was 1.5-fold enriched ($P_{adj} <$
355 0.0011) in the predicted cross-kingdom targets of MYC- and EPI-specific *B. hordei* milRNAs.
356 Two GO terms relating to protein K63-linked deubiquitination (GO:0070536 and
357 GO:0061578) were 80.9-fold enriched in the putative cross-kingdom targets of *B. hordei*
358 milRNAs enriched in MYC, EPI, and HAU ($P_{adj} < 0.05$). Only three *H. vulgare* milRNA cross-
359 kingdom target sets, containing MYC-specific, EPI-specific, or MYC- and EPI-specific milRNAs,
360 showed significant enrichment of GO terms (Figure 5B). Two genes targeted by MYC- and
361 EPI-specific milRNAs had the GO term "microtubule-severing ATPase activity" ($P_{adj} < 0.046$;
362 128.9-fold enrichment), while the term "vacuole" was 6.5-fold enriched in the same set (P_{adj}
363 < 0.004). In the MYC-specific set, "ADP binding" was 6.2-fold enriched ($P_{adj} < 0.04$) and
364 "nucleoside-triphosphatase activity" 5.1-fold ($P_{adj} < 0.02$); "ADP binding" was also enriched
365 in the EPI-specific set (11-fold, $P_{adj} < 0.009$). The only GO terms enriched in endogenous
366 milRNA targets of *B. hordei* were related to protein phosphorylation (Supplementary
367 Figure 11A), exhibiting 4-fold to 11-fold enrichment ($P_{adj} < 7e\text{-}10$) in MYC-, EPI-, MYC- and
368 EPI-, and MYC/EPI/HAU-specific sets. Conversely, we found 69 enriched GO terms in the sets
369 of putative endogenous *H. vulgare* target genes Supplementary Figure 11B; Supplementary
370 Table 12 and Supplementary Table 13). Many of these GO terms relate to regulatory, cell
371 cycle, growth, and developmental processes.
372 Altogether, we detected that most *B. hordei* and *H. vulgare* milRNAs exhibited site-specific
373 enrichment patterns, suggestive of their infection stage- and tissue-specific induction.
374 Among the putative targets of *B. hordei* milRNAs, genes coding for proteins involved in
375 protein phosphorylation appeared to be consistently overrepresented, both in presumed
376 endogenous and cross-kingdom gene targets. Predicted targets of *H. vulgare* milRNAs
377 showed some enrichment of processes related to microtubule-severing ATPase activity in
378 cross-kingdom *B. hordei* target genes, while endogenously regulating cell cycle, growth, and
379 development.
380
381 ***B. hordei* shows signs of phasing in coding genes and retrotransposons**

382 In addition to detecting milRNA candidates, ShortStack (29) can suggest loci containing
383 phased siRNAs (phasiRNAs). Unexpectedly, ShortStack detected that phasiRNAs had
384 occurred in RNAs from 22 *B. hordei* loci in our dataset, present in samples EPI and MYC but
385 none of the other samples (phasing score > 30). Of these, two were found in genes encoding
386 Sgk2 kinases (*BLGH_05411* and *BLGH_03674*), which are abundant in the genome of the
387 fungus (32), including at least one apparent pseudogenized Sgk2 kinase (*BLGH_03674*;
388 Figure 6, Supplementary Figure 12). Another four phasing loci corresponded to coding
389 genes, namely *BLGH_02275*, *BLGH_00530*, *BLGH_00532* (encoding proteins of unknown
390 function), and *BLGH_03506* (encoding CYP51/Eburicol 14-alpha-demethylase, involved in
391 ergosterol biosynthesis). The remaining 16 phasing loci were found to be in
392 retrotransposons (Supplementary Table 14). Since ShortStack is not optimized for phasiRNA
393 prediction (29), we used the PHASIS pipeline (33), unitas (34), and PhaseTank (35) to detect
394 evidence of phasing in the genome of *B. hordei* with our sRNA-seq dataset. PhaseTank failed
395 to predict any phasiRNAs with our data. However, we detected 153 putative phasing loci
396 with PHASIS, consisting of 21- or 22-base long phasiRNAs ($P < 0.0005$, Supplementary Table
397 14). We found that nine phasiRNA loci were located in coding genes of *B. hordei*, of which
398 seven encode Sgk2 kinases. Further, one coding gene subject to phasiRNA enrichment
399 (*BLGH_05762*) encoded a putative secreted protein, and another (*BLGH_00843*) a gene
400 encoding a protein of unknown function. Nineteen phasing loci were in the intergenic space.
401 The majority of phasiRNAs were found in retrotransposons of *B. hordei*, i.e., 42 *Tad*, 7
402 *HaTad*, 23 *Copia*, 29 *Gypsy*, and 23 *NonLTR* retrotransposons (Supplementary Table 14),
403 accounting for 124 loci altogether. One DNA transposon type *Mariner-2* and one unknown
404 transposon was found as well. The most sensitive detection method with our data was
405 unitas (34), which predicted 1,694 unique phasing loci in the genome of *B. hordei*
406 (Supplementary Table 14). These loci were randomly distributed on the scaffolds of
407 *B. hordei* (Figure 6A). Of these, 135 were located in coding genes and 1,535 in transposable
408 elements, while 24 loci were intergenic (Figure 6C). Of the coding genes, 67 encoded Sgk2
409 kinases, while seven encoded predicted secreted effector proteins. GO terms related to
410 protein phosphorylation and organonitrogen metabolism were enriched in this set of genes
411 (Figure 6D). The abundance of phasiRNAs in the different sites varied greatly; for example,
412 the reads mapping to the Sgk2 kinase locus *BLGH_03674* were abundant in the MYC and EPI
413 samples, while much less numerous in HAU and P40. Surprisingly, they were also very
414 abundant in the EV+ fraction (Supplementary Figure 12).
415
416
417

418 Discussion

419

420 In this work, we sought to characterise the spectrum of sRNAs present in the context of a
421 compatible barley-powdery mildew interaction by isolating and sequencing sRNAs from
422 different "sites" of infected leaves: the epiphytic fungal structures that include the
423 mycelium, runner hyphae, conidiophores and conidia (MYC), the infected barley epidermis
424 including plant tissue and the intracellular fungal haustoria (EPI), a fraction enriched of

425 fungal haustoria (HAU), microsomes obtained after lysis of the epidermal cells (P40), and
426 extracellular vesicles from the apoplast of non-infected (EV-) and infected (EV+) leaves.
427 The first aim was to determine whether the sRNAs differed between the sites. First, we
428 discovered abundant and highly specific fragments derived from 5.8S and 28S rRNA of
429 barley and *B. hordei*, and of tRNAs from *B. hordei* (rRFs and tRFs, respectively; Figure 2 and
430 Table 2). In most cases, these fragments were of discrete lengths (31-33 bases), derived
431 from the 3' end of the 5.8S rRNA, specific locations within the 28S rRNA, or represented
432 tRNA halves. The fragments exhibited highly specific and prominent enrichment at specific
433 sites of the interaction; thus, they are unlikely to be the product of random RNA
434 exonuclease degradation. Noncoding RNAs including tRNAs and rRNAs preferentially give
435 rise to terminal fragments in animals (36, 37), fungi (38), and plants (39). rRFs have been
436 shown to be involved in ageing in *Drosophila melanogaster* (40), rRNA degradation in
437 response to erroneous rRNAs and UV irradiation stress in *Caenorhabditis elegans* (41, 42),
438 and the response to pathogen infection in black pepper (*Piper nigrum*; (39). Many barley
439 rRFs were abundant in EV+ while not enriched in some EV- samples derived from
440 noninfected plants (Supplementary Figure 10), suggesting their biogenesis is induced by
441 fungal infection in barley. By contrast, *B. hordei* 5.8S rRNA-derived rRFs were particularly
442 abundant in isolated haustoria, suggestive of a role related to the intimate interaction with
443 the host plant.
444 tRFs appear to be involved in multiple regulatory processes in plants (43). They may play a
445 role in translation inhibition, since 5'-terminal oligoguanine-containing tRF halves of
446 *A. thaliana* can inhibit translation *in vitro* (44). They accumulate under various stresses
447 including phosphate starvation in barley and *A. thaliana* (45, 46) and *Fusarium graminearum*
448 infection in wheat (47). Further, tRNA halves and 10-16 base tiny tRFs represent substantial
449 portions of the sRNA pool in *A. thaliana* and may not be random tRNA degradation products
450 (48). We observed fungal rather than plant tRFs of 31-32 bases specifically in isolated
451 mycelium (Table 2). Some 28-35-base long tRFs are abundant in appressoria of the rice blast
452 pathogen *Magnaporthe oryzae* (49), suggesting infection stage- or tissue-specific roles for
453 these fragments in plant-pathogenic fungi. Intriguingly, the nitrogen-fixing bacterium
454 *Bradyrhizobium japonicus* exchanges specific tRFs with its host plant soybean, hijacking the
455 host RNAi machinery and supporting nodulation (50). While our data does not demonstrate
456 *B. hordei* 31-32 base tRF exchange with the host, we detected tRFs in both infected
457 epidermis and one EV- sample (Figure 2; Supplementary Figure 10), which hints at some
458 tRFs occurring in vesicles and infected host cells.
459 An important question is how such rRNA and tRNA fragments arise and how they are
460 specifically enriched in plants and fungi. Both rRFs and tRFs can be generated by Dicer and
461 loaded onto Ago. For example, 18-26 base long tRFs accumulate in a DCL1-dependent
462 manner and mediate Ago-driven cleavage of retrotransposons in *A. thaliana* (51), and 23-
463 base-long rRFs derived from the 5' end of 5.8S rRNA appear to be associated with AGO1 in
464 *P. nigrum* (39). In the fungus *Neurospora crassa*, the production of rRFs requires the RNA-
465 dependent RNA polymerase QDE-1, the helicase QDE-3, and DCL (38). However, the
466 fragments we observed were longer than 26 nucleotides. Thus, they are unlikely to be
467 associated with Dicer and Ago proteins. Instead, these specific tRFs and rRFs may have been
468 generated by specific RNases, like the RNase A Angiogenin in humans (52), the

469 *Saccharomyces cerevisiae* RNase T2 Rny1p (53), and plant RNase T2 (54–56, 47). RNase T2
470 most likely recognizes and hydrolyses single-stranded rRNA/tRNA loops, which could explain
471 why the ends of the tRFs and rRFs we observed are always found in single-stranded loops
472 (Figure 2). However, it is not clear why specific rRFs and tRFs accumulate while the
473 remaining rRNA and tRNA molecules disappear. We found that these fragments potentially
474 form novel secondary structures, which may render them inaccessible to RNA exonucleases,
475 and that the barley 5.8S rRF may be energetically more stable than other fragments derived
476 from the same molecule (Supplementary Figure 6). However, this is not the case for all rRFs
477 and tRFs we found, suggesting that predicted thermodynamic stability alone cannot explain
478 their high abundance. Future research will show if plants and pathogens repurposed specific
479 fragments of these evolutionary ancient rRNA and tRNA molecules specifically towards
480 intra- or cross-species communication.
481 Next, we turned our attention to miRNAs and milRNAs; in particular we attempted to
482 predict possible targets for endogenous and putative cross-kingdom gene regulation by
483 RNAi. We found that barley milRNAs are predicted to target more endogenous genes than
484 fungal genes (Figure 5), while *B. hordei* milRNAs are predicted to target more genes cross-
485 kingdom in barley. This trend was particularly evident in haustoria (76 of 108 milRNAs had
486 calculated cross-kingdom targets). The most frequent process associated with putative gene
487 targets for *B. hordei* milRNAs in samples derived from epiphytic mycelium and infected
488 epidermis is protein phosphorylation. Protein phosphorylation is important during plant
489 defence, especially for signal transduction (57). In support of this notion, kinases have been
490 reported as sRNA targets before. For example, *B. cinerea* sRNAs target *A. thaliana* MAP
491 kinases and cell wall-associated kinases (11). Similarly, sRNAs from the wheat stripe rust
492 *Puccinia striiformis* f.sp. *tritici* are predicted to target many kinase genes in wheat (58), and
493 *Fusarium oxysporum mil-R1* interferes with kinases of its host, tomato (59). Although fewer,
494 there are also potential cross-kingdom targets for barley milRNAs. For example, barley
495 milRNAs were predicted to target *B. hordei* genes related to microtubule-severing ATPase
496 activity, ADP binding, and nucleoside triphosphatase activity (Figure 5). Microtubules play
497 key roles in tip growth of hyphae in fungi, and the severing ATPase activity is essential for
498 microtubule organization (60, 61). It is therefore possible that plant miRNAs have evolved to
499 interfere with microtubule dynamics in the fungal pathogen.
500 Remarkably, we also detected *B. hordei* milRNAs in EV+ samples. These milRNAs are unlikely
501 to be contaminations because a considerable number (26 in total) of *B. hordei* milRNAs that
502 were specifically enriched in this sample type (Figure 4B). In principle, these EV+-enriched
503 *B. hordei* milRNAs could originate from *B. hordei*-derived microsomes. However, the
504 apoplastic space is physically separated from the main plant-fungus interaction site (the
505 interface between the extrahaustorial membrane and the plant cell wall) by the haustorial
506 neck band (62), which makes vesicle diffusion of fungal origin into the apoplast unlikely. In
507 principle, broken cells or breaking of cells or the haustorial neck during sample preparation
508 are another possibility for the origin of these EVs. Also, during the vacuum infiltration
509 process to obtain the apoplastic fluid, *B. hordei* EVs could be washed off the leaf surface and
510 the mycelium. However, there was limited co-enrichment of milRNAs in MYC and EV+
511 samples (Figure 4), and the EV+-specific milRNAs preclude this scenario. Therefore, it is
512 possible that *B. hordei* milRNAs hijack barley EVs in a similar manner as the turnip mosaic

513 virus does in *Nicotiana benthamiana* (63). The virus uses this mechanism to disperse its
514 genetic material. However, this scenario would require the transition of fungal sRNAs
515 through several stages of endo- and exocytosis.
516 PhasiRNAs have been well-documented in plants where they are thought to be the result of
517 complex processes of controlled degradation of double-stranded RNAs; they play roles in a
518 wide variety of biological functions including development and plant immunity (64).
519 Conversely, there is only very limited information about phasiRNA in fungi: to the best of
520 our knowledge the only case where phasiRNAs have been reported in the fungal kingdom is
521 *Sclerotinia sclerotiorum* infected by a hypovirus (8). We were, therefore, surprised to find a
522 clear signature of phasiRNA mapping to the fungal genome in *B. hordei* using ShortStack
523 (Figure 6). We subsequently succeeded in detecting phasiRNAs using two other independent
524 algorithms (unitas and PHASIS; Figure 6). The different pipelines detected somewhat
525 different sets of phased loci in the *B. hordei* genome, which likely reflects the different
526 mapping protocols. PHASIS exhibited the lowest overlap in phasing locations between the
527 three tools; this is probably because PHASIS does not use already existing mapping files but
528 performs its own mapping procedure instead. In any case, the low degree of overlap
529 highlights the suboptimal performance of these tools for the identification of phasiRNA in
530 filamentous fungi, and improvements may need to be implemented to determine complete
531 phasiRNA complements in these organisms. The vast majority of phasiRNAs mapped to
532 repetitive elements in the *B. hordei* genome, i.e., transposons and the previously described
533 abundant *Sgk2* kinase loci (32). This may result from the involvement of phasiRNAs in
534 controlling the expression of such genomic elements in the absence of the otherwise highly
535 conserved repeat-induced point mutation (RIP) pathway (65, 28). In animals, it is thought
536 that PIWI-associated RNAs (that show analogous phasing to plant phasiRNAs) also function
537 to control transposons in *Drosophila* (66). Nevertheless, according to our data, some
538 protein-coding gene loci in *B. hordei* show the presence of phased sRNAs as well, raising the
539 possibility that the expression of these genes may be subject to regulation by RNAi.
540 The presence of predicted phasiRNAs of fungal origin in EVs of the leaf apoplast from
541 infected barley leaves (EV+) is intriguing. It is difficult to rationalise what function, if any,
542 these may have in modulating plant gene expression at remote sites. We note, however,
543 that trans-acting small interfering RNA3a RNAs (tasi-RNA) derived from the *A. thaliana*
544 *TAS3a* locus and synthesized within three hours of pathogen infection may be an early
545 mobile signal in systemic acquired resistance (67). It is thus conceivable that trafficking of
546 sRNAs of fungal origin may follow the same route and may target plant gene expression
547 (24), and that fungal phasiRNAs in plant EVs are simply unintended by-products of this track.
548 Overall, our findings further support the notion that phasing exists in the fungal kingdom
549 and additionally provide evidence that transposable elements in *B. hordei* are subject to
550 sRNA-directed post-transcriptional regulation.
551
552
553

554 Material and Methods

555

556 **Plant cultivation**

557 Plants of barley (*H. vulgare* cv. Margret) were grown in SoMi513 soil (HAWITA, Vechta,
558 Germany) under a long day cycle (16 h light period at 23 °C, 8 h darkness at 20 °C) at 60-65%
559 relative humidity and 105-120 µmol s^{-1} m^{-2} light intensity. Seven-day-old barley plants were
560 inoculated with *B. hordei* strain K1; the plants were transferred to growth chambers with a
561 long day cycle (12 h light at 20 °C, 12 h dark at 19 °C) at ca. 60% relative humidity and 100
562 µmol s^{-1} m^{-2}.
563
564 **Isolation of small RNAs**
565 Seven-day-old barley was inoculated with *B. hordei* strain K1. At four days after inoculation,
566 the primary leaves were harvested to isolate mycelia, epiphytic, haustoria, and microsomes
567 from infected epidermis (P40). The dissection of the tissues and fractions was carried out as
568 previously described (68). Briefly, this consisted of dipping the excised leaves in cellulose
569 acetate (5% w/v in acetone), letting the acetone evaporate for a few minutes, peeling first
570 the epiphytic structures (MYC; this contained epiphytic mycelia, conidia and spores), then
571 dissecting the adaxial barley epidermis (EPI).
572 A portion of the epidermis samples were subsequently used to extract haustoria (HAU) and
573 epidermis microsomes (P40). First, the plant cell walls were digested by incubating the
574 epidermis in "Onozuka" R-10 cellulase (YAKULT pharmaceutical - Duchefa Biochemie BV,
575 Haarlem, The Netherlands; dissolved in 2% w/v in potassium vesicle isolation buffer; 20 mM
576 MES, 2 mM $CaCl_2$, 0.1 M KCl, pH 6.0; (69)) for 2 h at 28 °C on a rotary shaker (80 rpm). The
577 digested epidermis samples were then filtered through a 40 µm nylon mesh sieve and
578 centrifuged for 20 min at 200 *g*. The pellet containing the haustoria was resuspended in
579 260 µL potassium vesicle isolation buffer and stored at -80 °C (HAU); ~ 1 to 2 x 10^6 haustoria
580 were obtained per sample. The supernatant was centrifuged again at 10,000 *g* for 30 min at
581 4 °C, and the pellet discarded. The resulting supernatant was centrifuged one last time at
582 40,000 *g* at 4 °C for 1 h; the pellet containing the microsomes was stored at -80 °C (P40).
583 Apoplastic wash fluid was extracted from barley plants at three days after inoculation with
584 *B. hordei* strain K1. Trays of both inoculated and non-inoculated plants were covered with
585 lids and incubated prior to apoplastic wash fluid extraction. Approximately 30 g of leaf fresh
586 weight were collected and vacuum infiltrated with potassium vesicle isolation buffer. Excess
587 buffer was carefully removed and the leaves were placed with the cut ends down in 20 mL
588 syringes. The syringes were inserted into 50 mL centrifuge tubes. Apoplastic wash fluid was
589 collected at 400 *g* for 12 min at 4 °C. Cellular debris was first removed by passing the
590 apoplastic wash fluid through a 0.22 µm syringe filter and further by centrifugation at
591 10,000 *g* for 30 min at 4 °C. A crude extracellular vesicle fraction was isolated from
592 apoplastic wash fluid based on a previously established protocol (69). The apoplastic wash
593 fluid was centrifuged for 1 h at 40,000 *g* (4 °C) in a swinging bucket rotor to collect
594 extracellular vesicles (EV- and EV+). The extracellular vesicle pellet was resuspended in 50 µL
595 20 mM Tris-HCl (pH 7.5).
596 The MYC and EPI samples were ground in liquid nitrogen with quartz sand in a chilled pestle
597 and mortar and RNA was extracted from all samples using TRIzol (Thermo Scientific,
598 Schwerte, Germany) as described by the manufacturer. The RNA from all other samples
599 were extracted by resuspending the frozen samples directly into the TRIzol reagent, and
600 proceeding as described. The quantity and quality of the RNA was measured by

601 spectrophotometry (NanoDrop, Thermo Scientific) and spectrofluorimetry (Qubit, Thermo
602 Scientific).
603
604 **sRNA sequencing and data processing**
605 RNA samples were quantified via the Qubit RNA HS Assay (Thermo Scientific), and sized with
606 a High Sensitivity RNA ScreenTape (Agilent, Santa Clara, CA, USA). Library preparation was
607 performed with RealSeq-Dual as recommended by the manufacturer (RealSeq Biosciences,
608 Santa Cruz, CA, USA; (70)) with 100 ng of RNA for each sample. Half the volume of each
609 library was amplified by 20 cycles of polymerase chain reaction. Libraries from all samples
610 were pooled for sequencing in the same flow cell of a NextSeq single-end 75 nt reads run.
611 FastQ files were trimmed of adapter sequences by using Cutadapt (71) with the following
612 parameters: cutadapt -u 1 -a TGGAATTCTCGGGTGCCAAGG -m 15. We further performed
613 quality trimming of reads with Trimmomatic v0.39 (72). FASTQ read data were inspected
614 using FastQC v0.11.5 (Babraham Bioinformatics, Cambridge, UK). FASTQ/FASTA files were
615 parsed with SeqKit v2.1.0 (73).
616
617 **Read length distribution analysis**
618 We determined read length counts with custom BASH scripts and plotted these data using
619 ggplot2 v3.3.4 (Wickham 2009) in R v4.1.2 (R Core Team 2021). Reads were mapped to the
620 reference genomes of *H. vulgare* (Hordeum_vulgare.IBSC_v2; (27)) and *B. hordei* DH14 v4
621 (28) using bowtie within the ShortStack pipeline v3.8.5-1 (29). We used SAMtools v1.9 (74)
622 in conjunction with custom BASH scripts to parse read mapping statistics. Read counts by
623 genomic features, i.e., coding genes, transposable elements, and milRNA genes identified by
624 ShortStack, were determined using featureCounts v2.0.1 (76). *H. vulgar*e transposable
625 elements were identified with RepeatMasker v4.0.7 (http://www.repeatmasker.org) using
626 the repeat database version RepBase-20170127 and '-species Hordeum'. The data were
627 plotted with ggplot2 v3.3.4 (77) in R v4.1.2 (78).
628
629 **Read BLAST searches**
630 We used a custom python script to generate FASTA files containing reads of 21-22 bases, 31-
631 32 bases, and 32-33 bases, respectively, and then deduplicated reads using clumpify.sh of
632 the BBmap package (https://jgi.doe.gov/data-and-tools/software-tools/bbtools/). We
633 downloaded the ribosomal and transfer RNA molecules deposited in the RFAM database
634 (http://ftp.ebi.ac.uk/pub/databases/Rfam/CURRENT/fasta_files/) in October 2021. All reads
635 were aligned to the RFAM databases using MMSeqs2 v9.d36de (Steinegger and Söding
636 2017). Reads aligning to RF02543 (28S rRNA) were subsequently aligned to the 28S rRNA
637 sequences of *H. vulgare* (RNAcentral accession URS0002132C2A_4513) and *B. hordei*
638 (URS0002174482_62688), respectively. Read alignment coverage was determined via
639 BEDtools v2.25.0 (75). Bar graphs and histograms displaying these data were plotted with
640 ggplot2 v3.3.4 (77) in R v4.1.2 (78).
641
642 **Structure and free energy analysis of rRNA and tRNA fragments**
643 We obtained rRNA and tRNA structures predicted by R2DT from RNA central
644 (https://rnacentral.org) and visualized the structures with Forna (79). We further used

645 Vienna RNAfold v2.4.18 webserver (30) to calculate secondary structures and their
646 minimum free energy (MFE) of 5.8S rRNAs, rRNA, and tRNA fragments.
647
648 **Identification of milRNAs**
649 We used ShortStack pipeline v3.8.5-1 (29) to predict milRNAs in the genomes of *H. vulgare*
650 (Hordeum_vulgare.IBSC_v2; (27)) and *B. hordei* DH14 (28). Small RNAs with a Dicer Call cut-
651 off of N15 were considered as microRNA-like (milRNA) RNAs. We collected non-redundant
652 *B. hordei* and *H. vulgare* miRNAs and milRNAs in GFF and FASTA formats in Supplementary
653 files 2-5. featureCounts v2.0.1 (76) was used to determine milRNA locus-specific read
654 counts.
655
656 **Quantification and clustering of milRNA expression**
657 We first analysed similarities/differences between samples using several statistical
658 approaches. Non-metric multi-dimensional scaling (NMDS) collapses multidimensional
659 information into fewer dimensions and does not require normal distribution. The stress
660 value represented the statistical fit of the model for the data. Stress values equal to or
661 below 0.05 indicated a good model fit. We complemented the NMDS analysis with metric
662 multi-dimensional scaling (MDS), principal component (PC) analysis, and Pearson coefficient
663 correlation (PCC)-based hierarchical clustering. In addition, non-parametric rank-based
664 ANOSIM (analysis of similarity) tests were performed to determine statistical differences
665 between samples.
666 Weighted gene coexpression network analysis (WGCNA; (80)) was performed using read
667 counts mapping to milRNA loci. First, we filtered out the non-expressed genes (cut-off
668 TPM < 1), leaving 22,415 *H. vulgare* and 2,217 *B. hordei* milRNAs for the construction of the
669 coexpression networks. The scale-free network distribution required determination of the
670 soft threshold β (12 for *H. vulgare* and 16 for *B. hordei*) of the adjacency matrix. A module
671 correlation of 0.1 with either sample was the cut-off for identifying milRNAs enriched in the
672 samples MYC, EPI, HAU, P40, and EV+; we then refined assignment of milRNAs to samples at
673 >2.5-fold above average expression across samples. We used pairwise differential
674 expression analysis with DESeq2 (81), EdgeR (82), and limma-VOOM (83) to confirm the
675 overall expression trends of milRNAs from *H. vulgare* and *B. hordei*. Intersections were
676 analyzed by UpSetR plots using ComplexUpset (84).
677
678 **Small RNA target prediction and GO enrichment of milRNA target sets**
679 We used psRNAtarget (https://www.zhaolab.org/psRNATarget) Schema V2 2017 release
680 (31) at an expectation value cut-off of 2. We performed GO enrichment on putative milRNA
681 target gene sets using ShinyGO v0.75 (85); *P* values indicated were calculated via false
682 discovery rate (FDR) correction (P_{adj}). GO terms were summarized by removing redundant
683 GO terms with EMBL-EBI QuickGO (https://www.ebi.ac.uk/QuickGO/) on GO version 2022-
684 04-26 and REVIGO (86) with Gene Ontology database and UniProt-to-GO mapping database
685 from the EBI GOA project versions from November 2021.
686
687 **PhasiRNA and tasiRNA detection in *B. hordei***
688 We used ShortStack pipeline v3.8.5-1 (29), the PHASIS pipeline (33), unitas v1.7.0 (34), and
689 PhaseTank v1.0 (35) to detect evidence of phasing in the genome of *B. hordei* with our small

RNA-seq dataset. Detected phasing sites were concatenated to non-redundant phasing loci using BEDtools v2.25.0 (Quinlan and Hall 2010). Manual inspection of phasing loci was done using Integrative Genomics Viewer (87).

Author contributions

P.D.S. conceived and conceptualized the project, generated materials (HAU, P40, EPI, MYC), and performed initial analysis of the sRNA-seq data. S.K. contributed to initial data analysis and milRNA identification, performed read length distribution analysis in the samples from this study and published data, analysed milRNA expression data, contributed to GO enrichment analysis, did phasiRNA detection in *B. hordei*, and designed figures. M.S. contributed to milRNA identification, read length distribution analysis, secondary structure predictions of RNA fragments, weighted correlation network analysis of milRNAs, performed milRNA target predictions, and gene ontology enrichment analysis. H.T. generated materials from EV samples. S.K., H.T., and P.D.S. drafted the manuscript, all authors edited the document. P.D.S. and R.P. provided reagents, funds, and laboratory space. All authors read and agreed to the final version of the manuscript.

Data availability statement

The sRNA sequencing data are deposited at NCBI/ENA/DDBJ under project accession PRJNA809109; the SRA accessions are listed in Supplementary Table 1. The *B. hordei* and *H. vulgare* miRNAs and milRNAs are available in GFF format and FASTA format in Supplementary files 2-5.

Code availability statement

All computational tools and their versions are described in the respective methods sections, and were run in default mode with modifications indicated. Custom codes for our analysis pipeline are available at https://github.com/stefankusch/smallRNA_seq_analysis.

Acknowledgments

We thank Blake Meyers for advice on the usage of PHASIS, and members of the DFG-funded FOR5116 consortium for critical feedback. The analysis was performed with computing resources granted by RWTH Aachen University under project ID rwth0146.

Funding

P.D.S was funded by a research fellowship from the Leverhulme Trust (RF-2019-053), a research award by the Alexander von Humboldt Foundation (GBR 1204122 GSA), and a Theodore von Kármán Fellowship (RWTH Aachen). H.T. was supported by the RWTH Aachen scholarship for doctoral students. The work was further supported by the Deutsche Forschungsgemeinschaft (DFG, German Research Foundation) project number 433194101 [grant PA 861/22-1 to R.P.] in the context of the Forschergruppe consortium FOR5116 “exRNA” and project number 274444799 [grant 861/14-2 awarded to R.P.] in the context of

the DFG-funded priority program SPP1819 “Rapid evolutionary adaptation – potential and constraints”.

References

1. Ma X, Wiedmer J, Palma-Guerrero J. 2019. Small RNA bidirectional crosstalk during the interaction between wheat and *Zymoseptoria tritici*. Front Plant Sci 10:1669. doi:10.3389/fpls.2019.01669.
2. Wong-Bajracharya J, Singan VR, Monti R, Plett KL, Ng V, Grigoriev IV, Martin FM, Anderson IC, Plett JM. 2022. The ectomycorrhizal fungus *Pisolithus microcarpus* encodes a microRNA involved in cross-kingdom gene silencing during symbiosis. Proc Natl Acad Sci USA 119. doi:10.1073/pnas.2103527119.
3. Klesen S, Hill K, Timmermans MCP. 2020. Small RNAs as plant morphogens. Curr Top Dev Biol 137:455–480. doi:10.1016/bs.ctdb.2019.11.001.
4. Chen X, Rechavi O. 2022. Plant and animal small RNA communications between cells and organisms. Nat. Rev. Mol. Cell Biol. 23:185–203. doi:10.1038/s41580-021-00425-y.
5. Bologna NG, Voinnet O. 2014. The diversity, biogenesis, and activities of endogenous silencing small RNAs in *Arabidopsis*. Annu Rev Plant Biol 65:473–503. doi:10.1146/annurev-arplant-050213-035728.
6. Lee H-C, Li L, Gu W, Xue Z, Crosthwaite SK, Pertsemlidis A, Lewis ZA, Freitag M, Selker EU, Mello CC, Liu Y. 2010. Diverse pathways generate microRNA-like RNAs and Dicer-independent small interfering RNAs in fungi. Mol. Cell 38:803–814. doi:10.1016/j.molcel.2010.04.005.
7. Komiya R. 2017. Biogenesis of diverse plant phasiRNAs involves an miRNA-trigger and Dicer-processing. J Plant Res 130:17–23. doi:10.1007/s10265-016-0878-0.
8. Lee Marzano S-Y, Neupane A, Domier L. 2018. Transcriptional and small RNA responses of the white mold fungus *Sclerotinia sclerotiorum* to infection by a virulence-attenuating hypovirus. Viruses 10. doi:10.3390/v10120713.
9. Fire A, Xu S, Montgomery MK, Kostas SA, Driver SE, Mello CC. 1998. Potent and specific genetic interference by double-stranded RNA in *Caenorhabditis elegans*. Nature 391:806–811. doi:10.1038/35888.
10. Fukudome A, Fukuhara T. 2017. Plant dicer-like proteins: double-stranded RNA-cleaving enzymes for small RNA biogenesis. J Plant Res 130:33–44. doi:10.1007/s10265-016-0877-1.
11. Weiberg A, Wang M, Lin F-M, Zhao H, Zhang Z, Kaloshian I, Huang H-D, Jin H. 2013. Fungal small RNAs suppress plant immunity by hijacking host RNA interference pathways. Science 342:118–123. doi:10.1126/science.1239705.
12. Wang M, Weiberg A, Lin F-M, Thomma BPHJ, Huang H-D, Jin H. 2016. Bidirectional cross-kingdom RNAi and fungal uptake of external RNAs confer plant protection. Nat Plants 2:16151. doi:10.1038/nplants.2016.151.
13. Cai Q, Qiao L, Wang M, He B, Lin F-M, Palmquist J, Huang H-D, Jin H. 2018. Plants send small RNAs in extracellular vesicles to fungal pathogen to silence virulence genes. Science 360:1126-1129. doi:10.1126/science.aar4142.
14. He B, Hamby R, Jin H. 2021. Plant extracellular vesicles: Trojan horses of cross-kingdom warfare. FASEB Bioadv 3:657–664. doi:10.1096/fba.2021-00040.
15. Manocha MS, Shaw M. 1964. Occurrence of lomasomes in mesophyll cells of ‘Khapli’ wheat. Nature 203:1402–1403. doi:10.1038/2031402b0.

779 16. Skokos D, Le Panse S, Villa I, Rousselle JC, Peronet R, David B, Namane A, Mécheri S. 2001. Mast
780 cell-dependent B and T lymphocyte activation is mediated by the secretion of immunologically
781 active exosomes. J. Immunol. 166:868–876. doi:10.4049/jimmunol.166.2.868.
782 17. Segura E, Guérin C, Hogg N, Amigorena S, Théry C. 2007. $CD8^+$ dendritic cells use LFA-1 to
783 capture MHC-peptide complexes from exosomes in vivo. J. Immunol. 179:1489–1496.
784 doi:10.4049/jimmunol.179.3.1489.
785 18. Morelli AE, Larregina AT, Shufesky WJ, Sullivan MLG, Stolz DB, Papworth GD, Zahorchak AF,
786 Logar AJ, Wang Z, Watkins SC, Falo LD, Thomson AW. 2004. Endocytosis, intracellular sorting,
787 and processing of exosomes by dendritic cells. Blood 104:3257–3266. doi:10.1182/blood-2004-
788 03-0824.
789 19. Parolini I, Federici C, Raggi C, Lugini L, Palleschi S, Milito A de, Coscia C, Iessi E, Logozzi M,
790 Molinari A, Colone M, Tatti M, Sargiacomo M, Fais S. 2009. Microenvironmental pH is a key
791 factor for exosome traffic in tumor cells. J. Biol. Chem. 284:34211–34222.
792 doi:10.1074/jbc.M109.041152.
793 20. Woith E, Fuhrmann G, Melzig MF. 2019. Extracellular vesicles-connecting kingdoms. Int J Mol
794 Sci 20. doi:10.3390/ijms20225695.
795 21. Zand Karimi H, Baldrich P, Rutter BD, Borniego L, Zajt KK, Meyers BC, Innes RW. 2022.
796 Arabidopsis apoplastic fluid contains sRNA- and circular RNA-protein complexes that are
797 located outside extracellular vesicles. Plant Cell 34:1863–1881. doi:10.1093/plcell/koac043.
798 22. Liu M, Braun U, Takamatsu S, Hambleton S, Shoukouhi P, Bisson KR, Hubbard K. 2021.
799 Taxonomic revision of *Blumeria* based on multi-gene DNA sequences, host preferences and
800 morphology. Mycoscience 62:143–165. doi:10.47371/mycosci.2020.12.003.
801 23. Kusch S, Frantzeskakis L, Thieron H, Panstruga R. 2018. Small RNAs from cereal powdery mildew
802 pathogens may target host plant genes. Fungal Biol. 122:1050–1063.
803 doi:10.1016/j.funbio.2018.08.008.
804 24. Hunt M, Banerjee S, Surana P, Liu M, Fuerst G, Mathioni S, Meyers BC, Nettleton D, Wise RP.
805 2019. Small RNA discovery in the interaction between barley and the powdery mildew
806 pathogen. BMC Genomics 20:345. doi:10.1186/s12864-019-5947-z.
807 25. Hippe S. 1985. Ultrastructure of haustoria of *Erysiphe graminis* f. sp. *hordei* preserved by
808 freeze-substitution. Protoplasma 129:52–61. doi:10.1007/BF01282305.
809 26. An QL, Ehlers K, Kogel KH, van Bel AJE, Huckelhoven R. 2006. Multivesicular compartments
810 proliferate in susceptible and resistant MLA12-barley leaves in response to infection by the
811 biotrophic powdery mildew fungus. New Phytol. 172:563–576.
812 27. Mascher M, Gundlach H, Himmelbach A, Beier S, Twardziok SO, Wicker T, Radchuk V, Dockter C,
813 Hedley PE, Russell J, Bayer M, Ramsay L, Liu H, Haberer G, Zhang X-Q, Zhang Q, Barrero RA, Li L,
814 Taudien S, Groth M, Felder M, Hastie A, Simkova H, Stankova H, Vrana J, Chan S, Munoz-
815 Amatriain M, Ounit R, Wanamaker S, Bolser D, Colmsee C, Schmutzer T, Aliyeva-Schnorr L,
816 Grasso S, Tanskanen J, Chailyan A, Sampath D, Heavens D, Clissold L, Cao S, Chapman B, Dai F,
817 Han Y, Li H, Li X, Lin C, McCooke JK, Tan C, Wang P, Wang S, Yin S, Zhou G, Poland JA, Bellgard
818 MI, Borisjuk L, Houben A, Dolezel J, Ayling S, Lonardi S, Kersey P, Langridge P, Muehlbauer GJ,
819 Clark MD, Caccamo M, Schulman AH, Mayer KFX, Platzer M, Close TJ, Scholz U, Hansson M,
820 Zhang G, Braumann I, Spannagl M, Li C, Waugh R, Stein N. 2017. A chromosome conformation
821 capture ordered sequence of the barley genome. Nature 544:427–433.
822 doi:10.1038/nature22043.
823 28. Frantzeskakis L, Kracher B, Kusch S, Yoshikawa-Maekawa M, Bauer S, Pedersen C, Spanu PD,
824 Maekawa T, Schulze-Lefert P, Panstruga R. 2018. Signatures of host specialization and a recent
825 transposable element burst in the dynamic one-speed genome of the fungal barley powdery
826 mildew pathogen. BMC Genomics 19:27. doi:10.1186/s12864-018-4750-6.

827 29. Johnson NR, Yeoh JM, Coruh C, Axtell MJ. 2016. Improved placement of multi-mapping small
828 RNAs. G3 6:2103–2111. doi:10.1534/g3.116.030452.
829 30. Gruber AR, Lorenz R, Bernhart SH, Neuböck R, Hofacker IL. 2008. The Vienna RNA websuite.
830 Nucleic Acids Res 36:W70-4. doi:10.1093/nar/gkn188.
831 31. Dai X, Zhao PX. 2011. psRNATarget: A plant small RNA target analysis server. Nucleic Acids Res
832 39:W155-9. doi:10.1093/nar/gkr319.
833 32. Kusch S, Ahmadinejad N, Panstruga R, Kuhn H. 2014. *In silico* analysis of the core signaling
834 proteome from the barley powdery mildew pathogen (*Blumeria graminis* f.sp. *hordei*). BMC
835 Genomics 15:843. doi:10.1186/1471-2164-15-843.
836 33. Kakrana A, Li P, Patel P, Hammond R, Anand D, Mathioni SM, Meyers BC. 2017. PHASIS : A
837 computational suite for de novo discovery and characterization of phased, siRNA-generating
838 loci and their miRNA triggers. bioRxiv. doi:10.1101/158832.
839 34. Gebert D, Hewel C, Rosenkranz D. 2017. unitas: The universal tool for annotation of small RNAs.
840 BMC Genomics 18:644. doi:10.1186/s12864-017-4031-9.
841 35. Guo Q, Qu X, Jin W. 2015. PhaseTank: Genome-wide computational identification of phasiRNAs
842 and their regulatory cascades. Bioinformatics 31:284–286. doi:10.1093/bioinformatics/btu628.
843 36. Li Z, Ender C, Meister G, Moore PS, Chang Y, John B. 2012. Extensive terminal and asymmetric
844 processing of small RNAs from rRNAs, snoRNAs, snRNAs, and tRNAs. Nucleic Acids Res 40:6787–
845 6799. doi:10.1093/nar/gks307.
846 37. Chen Z, Sun Y, Yang X, Wu Z, Guo K, Niu X, Wang Q, Ruan J, Bu W, Gao S. 2017. Two featured
847 series of rRNA-derived RNA fragments (rRFs) constitute a novel class of small RNAs. PLoS One
848 12:e0176458. doi:10.1371/journal.pone.0176458.
849 38. Lee H-C, Chang S-S, Choudhary S, Aalto AP, Maiti M, Bamford DH, Liu Y. 2009. qiRNA is a new
850 type of small interfering RNA induced by DNA damage. Nature 459:274–277.
851 doi:10.1038/nature08041.
852 39. Asha S, Soniya EV. 2017. The sRNAome mining revealed existence of unique signature small
853 RNAs derived from 5.8SrRNA from *Piper nigrum* and other plant lineages. Sci Rep 7:41052.
854 doi:10.1038/srep41052.
855 40. Guan L, Grigoriev A. 2020. Age-related argonaute loading of ribosomal RNA fragments.
856 MicroRNA 9:142–152. doi:10.2174/2211536608666190920165705.
857 41. Zhou X, Feng X, Mao H, Li M, Xu F, Hu K, Guang S. 2017. RdRP-synthesized antisense ribosomal
858 siRNAs silence pre-rRNA via the nuclear RNAi pathway. Nat Struct Mol Biol 24:258–269.
859 doi:10.1038/nsmb.3376.
860 42. Zhu C, Yan Q, Weng C, Hou X, Mao H, Liu D, Feng X, Guang S. 2018. Erroneous ribosomal RNAs
861 promote the generation of antisense ribosomal siRNA. Proc Natl Acad Sci USA 115:10082–
862 10087. doi:10.1073/pnas.1800974115.
863 43. Alves CS, Nogueira FTS. 2021. Plant small RNA world growing bigger: tRNA-derived fragments,
864 longstanding players in regulatory processes. Front Mol Biosci 8:638911.
865 doi:10.3389/fmolb.2021.638911.
866 44. Lalande S, Merret R, Salinas-Giegé T, Drouard L. 2020. Arabidopsis tRNA-derived fragments as
867 potential modulators of translation. RNA Biol 17:1137–1148.
868 doi:10.1080/15476286.2020.1722514.
869 45. Hackenberg M, Huang P-J, Huang C-Y, Shi B-J, Gustafson P, Langridge P. 2013. A comprehensive
870 expression profile of microRNAs and other classes of non-coding small RNAs in barley under
871 phosphorous-deficient and -sufficient conditions. DNA Res 20:109–125.
872 doi:10.1093/dnares/dss037.

873 46. Hsieh L-C, Lin S-I, Shih AC-C, Chen J-W, Lin W-Y, Tseng C-Y, Li W-H, Chiou T-J. 2009. Uncovering
874 small RNA-mediated responses to phosphate deficiency in Arabidopsis by deep sequencing.
875 Plant Physiol 151:2120–2132. doi:10.1104/pp.109.147280.
876 47. Sun Z, Hu Y, Zhou Y, Jiang N, Hu S, Li L, Li T. 2022. tRNA-derived fragments from wheat are
877 potentially involved in susceptibility to Fusarium head blight. BMC Plant Biol 22:3.
878 doi:10.1186/s12870-021-03393-9.
879 48. Ma X, Liu C, Kong X, Liu J, Zhang S, Liang S, Luan W, Cao X. 2021. Extensive profiling of the
880 expressions of tRNAs and tRNA-derived fragments (tRFs) reveals the complexities of tRNA and
881 tRF populations in plants. Sci China Life Sci 64:495–511. doi:10.1007/s11427-020-1891-8.
882 49. Nunes CC, Gowda M, Sailsbery J, Xue M, Chen F, Brown DE, Oh Y, Mitchell TK, Dean RA. 2011.
883 Diverse and tissue-enriched small RNAs in the plant pathogenic fungus, *Magnaporthe oryzae*.
884 BMC Genomics 12:288. doi:10.1186/1471-2164-12-288.
885 50. Ren B, Wang X, Duan J, Ma J. 2019. Rhizobial tRNA-derived small RNAs are signal molecules
886 regulating plant nodulation. Science 365:919–922. doi:10.1126/science.aav8907.
887 51. Martinez G, Choudury SG, Slotkin RK. 2017. tRNA-derived small RNAs target transposable
888 element transcripts. Nucleic Acids Res 45:5142–5152. doi:10.1093/nar/gkx103.
889 52. Yamasaki S, Ivanov P, Hu G-F, Anderson P. 2009. Angiogenin cleaves tRNA and promotes stress-
890 induced translational repression. J. Cell Biol. 185:35–42. doi:10.1083/jcb.200811106.
891 53. Thompson DM, Parker R. 2009. The RNase Rny1p cleaves tRNAs and promotes cell death during
892 oxidative stress in *Saccharomyces cerevisiae*. J. Cell Biol. 185:43–50.
893 doi:10.1083/jcb.200811119.
894 54. Singh NK, Paz E, Kutsher Y, Reuveni M, Lers A. 2020. Tomato T2 ribonuclease LE is involved in
895 the response to pathogens. Mol Plant Pathol 21:895–906. doi:10.1111/mpp.12928.
896 55. Megel C, Hummel G, Lalande S, Ubrig E, Cognat V, Morelle G, Salinas-Giegé T, Duchêne A-M,
897 Maréchal-Drouard L. 2019. Plant RNases T2, but not Dicer-like proteins, are major players of
898 tRNA-derived fragments biogenesis. Nucleic Acids Res 47:941–952. doi:10.1093/nar/gky1156.
899 56. Alves CS, Vicentini R, Duarte GT, Pinoti VF, Vincentz M, Nogueira FTS. 2017. Genome-wide
900 identification and characterization of tRNA-derived RNA fragments in land plants. Plant Mol.
901 Biol. 93:35–48. doi:10.1007/s11103-016-0545-9.
902 57. Park C-J, Caddell DF, Ronald PC. 2012. Protein phosphorylation in plant immunity: Insights into
903 the regulation of pattern recognition receptor-mediated signaling. Front Plant Sci 3:177.
904 doi:10.3389/fpls.2012.00177.
905 58. Mueth NA, Ramachandran SR, Hulbert SH. 2015. Small RNAs from the wheat stripe rust fungus
906 (*Puccinia striiformis* f.sp. *tritici*). BMC Genomics 16:718. doi:10.1186/s12864-015-1895-4.
907 59. Ji H-M, Mao H-Y, Li S-J, Feng T, Zhang Z-Y, Cheng L, Luo S-J, Borkovich KA, Ouyang S-Q. 2021.
908 *Fol*-milR1, a pathogenicity factor of *Fusarium oxysporum*, confers tomato wilt disease resistance
909 by impairing host immune responses. New Phytol. doi:10.1111/nph.17436.
910 60. Horio T. 2007. Role of microtubules in tip growth of fungi. J Plant Res 120:53–60.
911 doi:10.1007/s10265-006-0043-2.
912 61. Roll-Mecak A, McNally FJ. 2010. Microtubule-severing enzymes. Curr. Opin. Cell Biol. 22:96–
913 103. doi:10.1016/j.ceb.2009.11.001.
914 62. Micali CO, Neumann U, Grunewald D, Panstruga R, O'Connell R. 2011. Biogenesis of a
915 specialized plant-fungal interface during host cell internalization of Golovinomyces orontii
916 haustoria. Cell Microbiol. 13:210–226.
917 63. Movahed N, Cabanillas DG, Wan J, Vali H, Laliberté J-F, Zheng H. 2019. Turnip Mosaic Virus
918 components are released into the extracellular space by vesicles in infected leaves. Plant
919 Physiol 180:1375–1388. doi:10.1104/pp.19.00381.

920 64. Liu Y, Teng C, Xia R, Meyers BC. 2020. PhasiRNAs in plants: Their biogenesis, genic sources, and
921 roles in stress responses, development, and reproduction. Plant Cell 32:3059–3080.
922 doi:10.1105/tpc.20.00335.
923 65. Spanu PD, Abbott JC, Amselem J, Burgis TA, Soanes DM, Stüber K, van Themaat EVL, Brown
924 JKM, Butcher SA, Gurr SJ, Lebrun MH, Ridout CJ, Schulze-Lefert P, Talbot NJ, Ahmadinejad N,
925 Ametz C, Barton GR, Benjdia M, Bidzinski P, Bindschedler LV, Both M, Brewer MT, Cadle-
926 Davidson L, Cadle-Davidson MM, Collemare J, Cramer R, Frenkel O, Godfrey D, Harriman J,
927 Hoede C, King BC, Klages S, Kleemann J, Knoll D, Koti PS, Kreplak J, Lopez-Ruiz FJ, Lu XL,
928 Maekawa T, Mahanil S, Micali C, Milgroom MG, Montana G, Noir S, O'Connell RJ, Oberhaensli S,
929 Parlange F, Pedersen C, Quesneville H, Reinhardt R, Rott M, Sacristan S, Schmidt SM, Schön M,
930 Skamnioti P, Sommer H, Stephens A, Takahara H, Thordal-Christensen H, Vigouroux M, Weßling
931 R, Wicker T, Panstruga R. 2010. Genome expansion and gene loss in powdery mildew fungi
932 reveal tradeoffs in extreme parasitism. Science 330:1543–1546.
933 66. Kotov AA, Adashev VE, Godneeva BK, Ninova M, Shatskikh AS, Bazylev SS, Aravin AA, Olenina
934 LV. 2019. piRNA silencing contributes to interspecies hybrid sterility and reproductive isolation
935 in *Drosophila melanogaster*. Nucleic Acids Res 47:4255–4271. doi:10.1093/nar/gkz130.
936 67. Shine MB, Zhang K, Liu H, Lim G-H, Xia F, Yu K, Hunt AG, Kachroo A, Kachroo P. 2022. Phased
937 small RNA-mediated systemic signaling in plants. Sci. Adv. 8:eabm8791.
938 doi:10.1126/sciadv.abm8791.
939 68. Li L, Collier B, Spanu P. 2019. Isolation of powdery mildew haustoria from infected barley. Bio
940 Protoc 9. doi:10.21769/BioProtoc.3299.
941 69. Rutter BD, Innes RW. 2017. Extracellular vesicles isolated from the leaf apoplast carry stress-
942 response proteins. Plant Physiol 173:728–741. doi:10.1104/pp.16.01253.
943 70. Barberán-Soler S, Vo JM, Hogans RE, Dallas A, Johnston BH, Kazakov SA. 2018. Decreasing
944 miRNA sequencing bias using a single adapter and circularization approach. Genome Biol.
945 19:105. doi:10.1186/s13059-018-1488-z.
946 71. Martin M. 2011. Cutadapt removes adapter sequences from high-throughput sequencing reads.
947 EMBnet j. 17:10. doi:10.14806/ej.17.1.200.
948 72. Bolger AM, Lohse M, Usadel B. 2014. Trimmomatic: A flexible trimmer for Illumina sequence
949 data. Bioinformatics 30:2114–2120. doi:10.1093/bioinformatics/btu170.
950 73. Shen W, Le S, Li Y, Hu F. 2016. SeqKit: A cross-platform and ultrafast toolkit for FASTA/Q file
951 manipulation. PLoS One 11:e0163962. doi:10.1371/journal.pone.0163962.
952 74. Li H, Handsaker B, Wysoker A, Fennell T, Ruan J, Homer N, Marth G, Abecasis G, Durbin R. 2009.
953 The Sequence Alignment/Map format and SAMtools. Bioinformatics 25:2078–2079.
954 doi:10.1093/bioinformatics/btp352.
955 75. Quinlan AR, Hall IM. 2010. BEDTools: A flexible suite of utilities for comparing genomic features.
956 Bioinformatics 26:841–842. doi:10.1093/bioinformatics/btq033.
957 76. Liao Y, Smyth GK, Shi W. 2014. featureCounts: An efficient general purpose program for
958 assigning sequence reads to genomic features. Bioinformatics 30:923–930.
959 doi:10.1093/bioinformatics/btt656.
960 77. Wickham H. 2009. ggplot2. Elegant graphics for data analysis. Use R. Springer, New York.
961 https://ebookcentral.proquest.com/lib/kxp/detail.action?docID=511468.
962 78. R Core Team. 2021. R: A language and environment for statistical computing. http://www.R-
963 project.org/.
964 79. Kerpedjiev P, Hammer S, Hofacker IL. 2015. Forna (force-directed RNA): Simple and effective
965 online RNA secondary structure diagrams. Bioinformatics 31:3377–3379.
966 doi:10.1093/bioinformatics/btv372.

967 80. Langfelder P, Horvath S. 2008. WGCNA: An R package for weighted correlation network
968 analysis. BMC Bioinformatics 9:559. doi:10.1186/1471-2105-9-559.
969 81. Love MI, Huber W, Anders S. 2014. Moderated estimation of fold change and dispersion for
970 RNA-seq data with DESeq2. Genome Biol. 15:550. doi:10.1186/s13059-014-0550-8.
971 82. Robinson MD, McCarthy DJ, Smyth GK. 2010. edgeR: A Bioconductor package for differential
972 expression analysis of digital gene expression data. Bioinformatics 26:139–140.
973 doi:10.1093/bioinformatics/btp616.
974 83. Law CW, Chen Y, Shi W, Smyth GK. 2014. voom: Precision weights unlock linear model analysis
975 tools for RNA-seq read counts. Genome Biol. 15:R29. doi:10.1186/gb-2014-15-2-r29.
976 84. Lex A, Gehlenborg N, Strobelt H, Vuillemot R, Pfister H. 2014. UpSet: Visualization of
977 intersecting sets. IEEE Trans Vis Comput Graph 20:1983–1992.
978 doi:10.1109/TVCG.2014.2346248.
979 85. Ge SX, Jung D, Yao R. 2020. ShinyGO: a graphical gene-set enrichment tool for animals and
980 plants. Bioinformatics 36:2628–2629. doi:10.1093/bioinformatics/btz931.
981 86. Supek F, Bošnjak M, Škunca N, Šmuc T. 2011. REVIGO summarizes and visualizes long lists of
982 gene ontology terms. PLoS One 6:e21800. doi:10.1371/journal.pone.0021800.
983 87. Robinson JT, Thorvaldsdóttir H, Wenger AM, Zehir A, Mesirov JP. 2017. Variant review with the
984 Integrative Genomics Viewer. Cancer Res 77:e31-e34. doi:10.1158/0008-5472.CAN-17-0337.
985 88. Steinegger M, Söding J. 2017. MMseqs2 enables sensitive protein sequence searching for the
986 analysis of massive data sets. Nat Biotechnol 35:1026–1028. doi:10.1038/nbt.3988.
987 89. Deng P, Le Wang, Cui L, Feng K, Liu F, Du X, Tong W, Nie X, Ji W, Weining S. 2015. Global
988 identification of microRNAs and their targets in barley under salinity stress. PLoS One
989 10:e0137990. doi:10.1371/journal.pone.0137990.
990 90. Wu L, Yu J, Shen Q, Huang L, Wu D, Zhang G. 2018. Identification of microRNAs in response to
991 aluminum stress in the roots of Tibetan wild barley and cultivated barley. BMC Genomics
992 19:560. doi:10.1186/s12864-018-4953-x.
993 91. Xin M, Wang Y, Yao Y, Song N, Hu Z, Qin D, Xie C, Peng H, Ni Z, Sun Q. 2011. Identification and
994 characterization of wheat long non-protein coding RNAs responsive to powdery mildew
995 infection and heat stress by using microarray analysis and SBS sequencing. BMC Plant Biol
996 11:61. doi:10.1186/1471-2229-11-61.
997 92. Ragupathy R, Ravichandran S, Mahdi MSR, Huang D, Reimer E, Domaratzki M, Cloutier S. 2016.
998 Deep sequencing of wheat sRNA transcriptome reveals distinct temporal expression pattern of
999 miRNAs in response to heat, light and UV. Sci Rep 6:39373. doi:10.1038/srep39373.
1000 93. Derbyshire M, Mbengue M, Barascud M, Navaud O, Raffaele S. 2019. Small RNAs from the plant
1001 pathogenic fungus *Sclerotinia sclerotiorum* highlight host candidate genes associated with
1002 quantitative disease resistance. Mol Plant Pathol 20:1279–1297. doi:10.1111/mpp.12841.
1003 94. Zhu C, Liu J-H, Zhao J-H, Liu T, Chen Y-Y, Wang C-H, Zhang Z-H, Guo H-S, Duan C-G. 2022. A
1004 fungal effector suppresses the nuclear export of AGO1-miRNA complex to promote infection in
1005 plants. Proc Natl Acad Sci USA 119:e2114583119. doi:10.1073/pnas.2114583119.
1006 95. Dunker F, Trutzenberg A, Rothenpieler JS, Kuhn S, Pröls R, Schreiber T, Tissier A, Kemen A,
1007 Kemen E, Hückelhoven R, Weiberg A. 2020. Oomycete small RNAs bind to the plant RNA-
1008 induced silencing complex for virulence. eLife 9:e56096. doi:10.7554/eLife.56096.
1009

1010 ## Figure legends
1011
1012 **Figure 1. Isolation of total RNA from six distinct sample types.** (**A**) We isolated total RNA
1013 from the following biological materials of *B. hordei*-infected barley leaves at four days after
1014 inoculation: (1) Epiphytic fungal mycelium (MYC), (2) infected epidermis without mycelium
1015 (EPI), (3) fungal haustoria (HAU), (4) microsomes of the epidermis depleted of haustoria
1016 (P40). In addition, we isolated total RNA from (5) apoplastic extracellular vesicles of infected
1017 plants (EV+) at three days after inoculation, and (6) apoplastic extracellular vesicles from
1018 non-infected control plants (EV-). The figure was created using bioRender.com. (**B**)
1019 Bioinformatic pipeline for sRNA-seq data analysis. We analysed the sRNA-seq reads in three
1020 ways: (1) by read size and read mapping distribution to the respective genomes, followed by
1021 read BLAST against the RFAM database for particular fractions of the read data; (2) by
1022 ShortStack analysis to detect putative milRNAs in both organisms, followed by principal
1023 component analysis for sample clustering, milRNA expression analysis, milRNA target
1024 prediction, and functional description of these targets by GO assignment; (3) by detection of
1025 loci enriched with predicted phasiRNAs.
1026
1027 **Figure 2. Specific barley 5.8S rRNA- and *B. hordei* tRNA-derived sRNAs are enriched in the**
1028 **31-33 base reads.** We aligned sRNA-seq reads of 31-33 bases in length to the RFAM
1029 database using MMSeqs2 (88). (**A**) The stacked bar graph shows the percentage of reads
1030 identified as 5S, 5.8S, 18S (small subunit, SSU), 28S (large subunit, LSU), or tRNA, as
1031 indicated in the color-coded legend. Green, reads identified as derived from *H. vulgare*;
1032 blue, reads identified as derived from *B. hordei* DH14; grey, reads not assigned to either
1033 *H. vulgare* or *B. hordei*; purple, reads identified as *B. hordei* tRNA-derived. Epiphytic fungal
1034 mycelium (MYC), infected epidermis without mycelium (EPI), fungal haustoria (HAU),
1035 microsomes of the epidermis without haustoria (P40), apoplastic extracellular vesicles (EV+),
1036 and apoplastic extracellular vesicles of non-infected control plants (EV-). The total number
1037 of reads assigned to each sample is given below the bar graph (visualized by circle size). (**B**)
1038 Predicted secondary structure of the barley 5.8S rRNA (RFAM accession
1039 CAJW010993076.1:c203-48; RNA central accession URS0000C3A4AE_112509), calculated by
1040 R2DT in RNA central (https://rnacentral.org) and visualized with Forna (79). The RNA
1041 sequence in orange indicates the over-represented 3' end in the reads from the EPI and EV+
1042 samples. (**C**) Histogram showing the number of reads (Read counts, x-axis) accounting for
1043 the *B. hordei* tRNA-derived reads in the sample MYC. The coding amino acid and respective
1044 mRNA codons are indicated on the left. The orange portion of the histogram bars indicates
1045 the fraction of reads coming from the three most abundant tRNA fragments. (**D**) The three
1046 most abundant tRNAs represented in the MYC sample are shown; left, Gln tRNA with UUG
1047 anticodon; middle, Gln tRNA with CUG anticodon; right, Glu tRNA with UUC anticodon. The
1048 orange-labelled sequences indicate the abundant tRNA fragments.
1049
1050 **Figure 3. The milRNA content of microsomal samples differs from mycelial, epidermal, and**
1051 **haustorial samples.** (**A**) and (**B**). We used non-metric multi-dimensional scaling (NMDS),
1052 which collapses multidimensional information into two dimensions to visualize sample
1053 similarity. Each data point represents the collapsed milRNA expression data from *H. vulgare*

1054 (**A**) and *B. hordei* (**B**). Blue, epiphytic fungal mycelium (MYC); green, infected epidermis
1055 without mycelium (EPI); light blue, fungal haustoria (HAU); purple, microsomes of the
1056 epidermis without haustoria (P40); orange, apoplastic extracellular vesicles (EV+); grey,
1057 apoplastic extracellular vesicles of non-infected control plants (EV-). (**C**) and (**D**) milRNA
1058 sample distances based on a Pearson correlation matrix from the milRNA expression data.
1059 The pair-wise Pearson correlations were used to calculate a Euclidean distance tree with all
1060 samples for *H. vulgare* (**C**) and *B. hordei* (**D**).
1061
1062 **Figure 4. Large sets of milRNAs exhibit site-specific distribution.** We calculated site-specific
1063 abundance in MYC, EPI, HAU, P40, and EV+ samples for (**A**) *H. vulgare* and (**B**) *B. hordei* using
1064 WGCNA and assigned milRNAs to samples exhibiting >2.5-fold enrichment over the average.
1065 The bottom panels indicate the set sizes of milRNAs in the respective samples (bar graph,
1066 left); blue, epiphytic fungal mycelium (MYC); green, infected epidermis without mycelium
1067 (EPI); light blue, fungal haustoria (HAU); purple, microsomes of the epidermis without
1068 haustoria (P40); orange, apoplastic extracellular vesicles (EV+). The dots indicate the
1069 samples contributing to the respective interaction sets. The second panels from the bottom
1070 are bar graphs of the intersection numbers, which are the numbers of milRNAs in the
1071 exclusive intersections. The third panels from the bottom show the normalized abundance
1072 of the milRNAs in the respective interaction sets as violin plot; the maximum TPM value
1073 across samples was used for each data point. The top panels are stacked bar charts of the
1074 sum of predicted milRNA target genes in *B. hordei* (blue) and *H. vulgare* (green); *B. hordei*
1075 genes encoding a secreted protein are shown in orange.
1076
1077 **Figure 5. GO enrichment analysis of putative cross-kingdom milRNA targets.** We
1078 determined all putative targets of the sets of *B. hordei* and *H. vulgare* milRNAs via
1079 psRNAtarget (31). We used ShinyGO v0.75 (85) to calculate enriched gene ontology (GO)
1080 terms in all milRNA target sets and summarized redundant GO terms with EMBL-EBI
1081 QuickGO (https://www.ebi.ac.uk/QuickGO/) on GO version 2022-04-26 and REVIGO (86). (**A**)
1082 GO enrichment terms found in putative cross-kingdom targets of *B. hordei* milRNAs in
1083 *H. vulgare*. (**B**) GO enrichment terms found in putative cross-kingdom targets of *H. vulgare*
1084 milRNAs in *B. hordei*. The GO terms and identifiers are indicated next to the bubble plots.
1085 Bubble size indicates fold enrichment of the term in the respective subset, fill color indicates
1086 -Log10 of the FDR-adjusted enrichment *P* value. The milRNA subsets are indicated below the
1087 bubble plots (see Figure 4 for all subsets). The icons on top of the plot were created with
1088 bioRender.com; the blue mycelium indicates *B. hordei* and the green plant barley.
1089
1090 **Figure 6. Transposable elements and genes encoding Sgk2 kinases are subject to phasing**
1091 **in *B. hordei*.** We identified phasiRNA-rich loci indicative of phasing in the genome of
1092 *B. hordei* with ShortStack pipeline v3.8.5-1 (29), the PHASIS pipeline (33), and unitas v1.7.0
1093 (34). (**A**) Global distribution of predicted phasing loci in the genome of *B. hordei* DH14 (28).
1094 The x-axis shows the genome position in mega base pairs (Mbp) and the scaffolds are
1095 indicated on the y-axis. Triangles denote loci in which phasiRNAs were found with unitas.
1096 Blue triangles, phasing loci coinciding with annotated coding genes; orange triangles,
1097 phasing loci coinciding with transposable elements; grey triangles, intergenic phasing loci.
1098 (**B**) Example of one phased locus in *B. hordei*, containing the gene *BLGH_03674*, the partial
1099 open reading frame of a gene encoding a Sgk2 kinase. A subset of representative samples
1100 from sites where phasing in this locus was detected is shown (EPI, MYC, and EV+), the full

set of samples is displayed in Supplementary Figure 12. From top to bottom, the position on the scaffold, scaffold name and window, gene and transposable element annotations, and sample names are indicated. Red lines indicate reads mapping in sense orientation of the displayed sequence window; blue lines show reads mapping in antisense orientation. A zoom-in is shown on the right. The putative trans-activating RNA (tasiRNA) is indicated with an asterisk. The figure was generated after inspection with Integrative Genome Viewer (IGV; (87)). (**C**) Bar graph summarizing the number of phasing loci types. The x-axis indicates the locus type, i.e., coding gene, transposon, or intergenic; the y-axis shows the number of loci. (**D**) GO enrichment of phased coding genes was calculated with ShinyGO v0.75 (85); terms were summarized to non-redundant GO terms with EMBL-EBI QuickGO (https://www.ebi.ac.uk/QuickGO/) on GO version 2022-04-26 and REVIGO (86). The bubble size indicates fold enrichment of the term in the respective subset, fill color indicates -Log10 of the FDR-adjusted enrichment *P* value. (**E**) A Venn diagram summarizing the overlap of discovered phasing loci with the three methods.

Tables

Table 1. Barley and *B. hordei* sRNAs (rRFs) derived from the 3'-end of the respective 5.8S rRNA.

			H. vulgare			***B. hordei***		
Sample	Peak [bases]	Number of reads	5.8S rRNA	3'-fragment *Hvu*-rRF0001	[%]	5.8S rRNA	3'-fragment *Bho*-rRF0001	[%]
MYC	31-32	5,667,110	4,984	4,719	94.7	1,210,651	1,205,821	99.6
EPI	32-33	37,604,028	30,810,544	30,592,716	99.3	888,803	831,512	93.4
HAU	31-32	8,489,360	809,111	763,391	94.3	2,218,412	1,740,772	78.5
P40	31-32	11,704,109	1,765,971	1,573,893	89.1	135,087	56,148	41.6
EV+	31-32	28,470,676	22,961,242	22,634,275	98.6	602,961	576,768	95.7
EV-	31-32	3,330,270	979,231	965,541	98.6	450,299	448,041	99.5

Table 2. Characteristic *H. vulgare* and *B. hordei* RNA fragments derived from tRNA (tRF) and rRNA (rRF).

Fragment	**Sequence (5'-3')**	**Species**	**RNA**	**Sample**
***Hvu*-rRF0001**	CGGCCGAGGGCACGCCUGCCUGGGCGUCA	*H. vulgare*	5.8S rRNA	EPI, EV+, EV-
***Hvu*-rRF0002**	CCGGAGGUAGGGUCCAGUGGCCGGAAGAGCA	*H. vulgare*	28S rRNA	HAU, P40
***Hvu*-rRF0003**	CGCGACGGGGCAUUGUAAGUGGCAGAGUGGCC	*H. vulgare*	28S rRNA	EPI, EV+, EV-
***Hvu*-rRF0004**	CAGGUCUCCAAGGUGAACAGCCUCUGGCCAA	*H. vulgare*	28S rRNA	EV+
***Hvu*-rRF0005**	GCUCGGGGGUCCCGGCCCCGAACCCGUCGGC	*H. vulgare*	28S rRNA	EV-
***Bho*-rRF0001**	UUCCCAGGGGCAUGCCUGUUCGAGCGUCC	*B. hordei*	5.8S rRNA	HAU
***Bho*-rRF0002**	UCUUUGAACGCACAUUGCGCCCCUGGGA	*B. hordei*	5.8S rRNA	HAU
***Bho*-rRF0003**	GUUACGGGCCCGAGUUGUAAUUUGUAGAAGAU	*B. hordei*	28S rRNA	MYC, EPI, HAU
***Bho*-rRF0004**	AAGCGUGUUACCCAUACUUCACCGCCCGGGUA	*B. hordei*	28S rRNA	HAU, P40
***Bho*-tRF0001**	GGUUGAUUAGUGUAGUUGGUUAUCACAUCGGA	*B. hordei*	tRNA	MYC
***Bho*-tRF0002**	GGCCAGUUGGUGUAAUGGUCAGCACGUCGGA	*B. hordei*	tRNA	MYC
***Bho*-tRF0003**	CGGAGAGCCCCGGGUUCGAUUCCCGGAUGCG	*B. hordei*	tRNA	MYC

1128 ## Supplementary Figure legends
1129
1130 **Supplementary Figure 1. Each sample type exhibits a distinctive sRNA read size**
1131 **distribution.** (**A**) We determined the sRNA read counts for read lengths between 15 and 40
1132 bases and plotted the read length (x-axis) against the respective number of reads (y-axis).
1133 Three replicates were analyzed for each of our six sample types: Epiphytic fungal mycelium
1134 (MYC), infected epidermis without mycelium (EPI), fungal haustoria (HAU), microsomes of
1135 the epidermis without haustoria (P40), apoplastic extracellular vesicles (EV+), and apoplastic
1136 extracellular vesicles of non-infected control plants (EV-). (**B**) We mapped sRNA sequencing
1137 reads of 15 and 40 bases long to the reference genomes of *H. vulgare* IBSCv2 (27) and *B.*
1138 *hordei* DH14 (28). The stacked bar graph shows the read counts (y-axis) for the respective
1139 read size (x-axis) from the three replicates. Green, reads mapping to the *H. vulgare* genome;
1140 blue, reads mapping to the *B. hordei* DH14 genome; grey, reads that did not map to either
1141 of the two genomes.
1142
1143 **Supplementary Figure 2. The majority of reads mapping to *B. hordei* or *H. vulgare***
1144 **originate from transposable elements or coding genes.** We assigned reads aligning to the
1145 genomes of (**A**) *B. hordei* or (**B**) *H. vulgare* to the features mRNA (coding genes; light
1146 blue/green), milRNA loci identified in this study (blue/green), and transposable elements
1147 (dark blue/green). We plotted the read length (x-axis) against the respective number of
1148 reads (y-axis). The six sample types were epiphytic fungal mycelium (MYC), infected
1149 epidermis without mycelium (EPI), fungal haustoria (HAU), microsomes of the epidermis
1150 without haustoria (P40), apoplastic extracellular vesicles (EV+), and apoplastic extracellular
1151 vesicles of non-infected control plants (EV-).
1152
1153 **Supplementary Figure 3. A broad range of reads originates from rRNAs in haustoria and**
1154 **microsomal fractions.** (**A**) We aligned all reads to the 5.8S (red), 18S (blue), and 28S (green)
1155 rDNA sequences of *B. hordei* and *H. vulgare*. The stacked bar graph shows the read counts
1156 (y-axis) for the respective read size (x-axis) from the three replicates. Three replicates were
1157 analyzed for each of our six sample types: Epiphytic fungal mycelium (MYC), infected
1158 epidermis without mycelium (EPI), fungal haustoria (HAU), microsomes of the epidermis
1159 without haustoria (P40), apoplastic extracellular vesicles (EV+), and apoplastic extracellular
1160 vesicles of non-infected control plants (EV-). Colors indicate reads aligning to the different
1161 rDNAs: Light blue, *B. hordei* 18S rDNA (RNAcentral accession URS000021D3E6_2867405);
1162 dark blue, *H. vulgare* 18S rDNA (URS0000AF30DE_112509); light green, *B. hordei* 28S rDNA
1163 (URS0002174482_62688); dark green, *H. vulgare* 28S rDNA (URS000212856A_112509); light
1164 red, *B. hordei* 5.8S rDNA (URS00006663F0_546991); dark red, *H. vulgare* 5.8S rDNA
1165 (URS0000C3A4AE_112509); grey, reads that did not align with any rDNA sequence. (**B**)
1166 Alignment of sRNA sequencing reads of 27-32 bases in length from HAU to the *B. hordei* 5.8S
1167 rDNA (154 bases in length). The graph shows the cumulative number of reads from the
1168 three replicates (y-axis) mapping to each position of the *B. hordei* 5.8S rDNA (x-axis). (**C**)
1169 Secondary structure of the *B. hordei* 5.8S rRNA (RFAM accession CAUH01009408.1:1222-
1170 1375; RNA central accession URS00006663F0_546991) predicted by R2DT in RNA central

1171 (https://rnacentral.org) and visualized with Forna (79). The RNA sequences in orange
1172 indicates the over-represented 3' end in the reads from the HAU sample.
1173
1174 **Supplementary Figure 4. Specific barley 28S rRNA-derived sRNAs are enriched in the 31-33**
1175 **base long reads.** (**A**) We aligned sRNA sequencing reads of 31-33 bases in length to the
1176 *H. vulgare* 28S rDNA (3,853 bases in length). The graphs display the number of reads
1177 identified (y-axis) mapping to each position of the barley 28S rDNA (x-axis). Epiphytic fungal
1178 mycelium (MYC), infected epidermis without mycelium (EPI), fungal haustoria (HAU),
1179 microsomes of the epidermis without haustoria (P40), apoplastic extracellular vesicles (EV+),
1180 and apoplastic extracellular vesicles of non-infected control plants (EV-). (**B**) Secondary
1181 structure of the 28S rRNA of *H. vulgare* (RFAM accession CAJW010993076.1:203-48; RNA
1182 central accession URS000212856A_112509) predicted by R2DT in RNA central
1183 (https://rnacentral.org). The sequence stretches shown in orange indicate the over-
1184 represented 28S rRNA fragments *Hvu*-rRF0002 and *Hvu*-rRF0003 from the HAU and P40
1185 samples. *Hvu*-rRF0003 fragments were also detected in EV+ and EV- samples, in addition to
1186 *Hvu*-rRF0004 and *Hvu*-rRF0005. (**C**) Sequences of the enriched 28S rRNA fragments of *H.*
1187 *vulgare* in FASTA format.
1188
1189 **Supplementary Figure 5. Specific *B. hordei* 28S rRNA-derived sRNAs are enriched in the 31-**
1190 **33 bases long reads.** (**A**) We aligned sRNA sequencing reads of 31-33 bases to the *B. hordei*
1191 28S rDNA (3,564 bases). The graphs display the number of reads identified (y-axis) mapping
1192 to each position of the *B. hordei* 28S rDNA (x-axis). Epiphytic fungal mycelium (MYC),
1193 infected epidermis without mycelium (EPI), fungal haustoria (HAU), microsomes of the
1194 epidermis without haustoria (P40), apoplastic extracellular vesicles (EV+), and apoplastic
1195 extracellular vesicles of non-infected control plants (EV-). (**B**) Secondary structure of the 28S
1196 rRNA of *B. hordei* (RFAM accessions CAUH01009223.1:1667-1 and CAUH01013050.1:1126-1;
1197 RNA central accession URS0000C6B9A3_546991; full structure was reconstructed from
1198 these partial fragments) predicted by R2DT in RNA central (https://rnacentral.org). The RNA
1199 stretches shown in orange indicate the over-represented 28S rRNA fragments *Bho*-rRF0003
1200 and *Bho*-rRF0004 from the Myc, Epi, Hau, and P40 samples. The fragment *Hvu*-rRF0004 is
1201 indicated in the EV+ plot. (**C**) DNA sequences of the enriched 28S rRNA of *B. hordei*
1202 fragments in FASTA format. (**D**) Pairwise alignment between *Hvu*-rRF0004 and the
1203 respective orthologous *B. hordei* 28S rDNA sequence. Positions in dark blue indicate
1204 identity, positions in light blue mismatches between the two sequences. Numbers above the
1205 alignment indicate alignment position, numbers on the left the position in the respective
1206 rDNA sequence of *H. vulgare* and *B. hordei*. The sequence covered by *Hvu*-rRF0004 is
1207 indicated below the alignment.
1208
1209 **Supplementary Figure 6. Predicted secondary structures of rRNA and tRNA fragments and**
1210 **their minimum free energies.** We used the Vienna RNAfold v2.4.18 webserver (30) to
1211 calculate secondary structures and their minimum free energy (MFE) of *H. vulgare* and
1212 *B. hordei* 5.8S rRNA (**A**), 28S rRNA (**B**), and tRNA (**C**) fragments. (**D**) The cartoon of the 5.8S
1213 rRNA structure indicates the position of the respective fragments; orange fragments
1214 indicate rRNA and tRNA fragments detected in our sRNA-seq dataset (Table 2) and blue

1215 fragments indicate theoretical fragments of identical or similar length used for comparison.
1216 The minimum free energies are indicated for each fragment.
1217
1218 **Supplementary Figure 7. Read length distribution profiles vary between sRNA-seq**
1219 **datasets.** We downloaded publicly available sRNA-seq datasets from the NCBI SRA database
1220 at https://www.ncbi.nlm.nih.gov/sra (accessions summarized in Supplementary Table 8) and
1221 analyzed the read length profiles of reads between 15 and 40 bases in length. The x-axis
1222 shows number of reads and the y-axis the read length in bases. We examined datasets from
1223 the following samples: (**A**) *H. vulgare* infected with *B. hordei* at 0, 24, and 48 hpi (24); (**B**)
1224 *H. vulgare* under salt stress (89) and aluminium stress (90), respectively; (**C**) *Triticum*
1225 *aestivum* (wheat) after infection with *B. graminis* f.sp. *tritici* at 12 hpi and under 40 °C heat
1226 stress (91); (**D**) *T. aestivum* infected with *Zymoseptoria tritici* at 12 dpi (1); (**E**) *T. aestivum*
1227 under 37 °C heat stress, continuous light stress, or UV treatment stress (92); (**F**) *Glycine max*
1228 (soybean) during nodulation with the bacterial species *Bradyrhizobium japonicum* at 10 and
1229 20 days after inoculation (50); (**G**) *Arabidopsis thaliana* and *Phaseolus vulgaris* (common
1230 bean) during infection with *Sclerotinia sclerotiorum* (93); (**H**) *A. thaliana* after infection with
1231 *Verticillium dahliae* and the *V. dahliae* mutant *aly1 aly2* (94); (**I**) *A. thaliana* infected with
1232 *Hyaloperonospora arabidopsidis* at 3, 4, and 7 dpi (95); (**J**) *Botrytis cinerea* cultivated *in vitro*
1233 (11); (**K**) *A. thaliana* infected with *B. cinerea* at 24, 48, and 72 hpi (11).
1234
1235 **Supplementary Figure 8. Most sRNA-seq datasets do not exhibit read length-specific**
1236 **enrichment of rRNA fragments.** We downloaded publicly available sRNA-seq datasets from
1237 the NCBI SRA database at https://www.ncbi.nlm.nih.gov/sra (accessions summarized in
1238 Supplementary Table 8) and aligned all reads against the respective 5.8S, 18S, and 28S rDNA
1239 sequences of each species. The stacked bar graph shows the read counts (y-axis) for the
1240 respective read size (x-axis) from all available replicates. Colors indicate reads aligning to the
1241 different rDNAs: Light blue, plant 18S rDNA; dark blue, fungal 18S rDNA or bacterial 16S
1242 rDNA; light green, plant 28S rDNA; dark green, fungal 28S rDNA or bacterial 23 rDNA; light
1243 red, plant 5.8S rDNA; dark red, fungal 5.8S rDNA or bacterial 5S rDNA; grey, reads that did
1244 not align with any rDNA sequence. We examined datasets from the following samples: (**A**)
1245 *H. vulgare* infected with *B. hordei* at 0, 24, and 48 hpi (24); (**B**) *H. vulgare* under salt stress
1246 (89) and aluminium stress (90), respectively; (**C**) *Triticum aestivum* (wheat) after infection
1247 with *B. graminis* f.sp. *tritici* at 12 hpi and under 40 °C heat stress (91); (**D**) *T. aestivum*
1248 infected with *Zymoseptoria tritici* at 12 dpi (1); (**E**) *T. aestivum* under 37 °C heat stress,
1249 continuous light stress, or UV treatment stress (92); (**F**) *Glycine max* (soybean) during
1250 nodulation with the bacterial species *Bradyrhizobium japonicum* at 10 and 20 days after
1251 inoculation (50); (**G**) *Arabidopsis thaliana* and *Phaseolus vulgaris* (common bean) during
1252 infection with *Sclerotinia sclerotiorum* (93); (**H**) *A. thaliana* after infection with *Verticillium*
1253 *dahliae* and the *V. dahliae* mutant *aly1 aly2* (94); (**I**) *A. thaliana* infected with
1254 *Hyaloperonospora arabidopsidis* at 3, 4, and 7 dpi (95); (**J**) *Botrytis cinerea* cultivated *in vitro*
1255 (11); (**K**) *A. thaliana* infected with *B. cinerea* at 24, 48, and 72 hpi (11).
1256
1257 **Supplementary Figure 9. Clustering of sRNA-seq samples.** We used NMDS, PCC (Figure 3),
1258 MDS (**A** and **B**), and PCA (**C** and **D**) to estimate sample differences and similarities. Each data
1259 point represents the collapsed milRNA expression data from one sample. Blue, epiphytic
1260 fungal mycelium (MYC); green, infected epidermis without mycelium (EPI); light blue, fungal
1261 haustoria (HAU); purple, microsomes of the epidermis without haustoria (P40); orange,

1262 apoplastic extracellular vesicles (EV+); grey, apoplastic extracellular vesicles of non-infected
1263 control plants (EV-).
1264
1265 **Supplementary Figure 10. EV- replicate three is more similar to EV samples from infected**
1266 ***H. vulgare* leaves.** (**A**) Read length profiles for the three apoplastic extracellular vesicles of
1267 non-infected control plants (EV-) generated in this study. The histograms show the read
1268 counts (y-axis) for the respective read size (x-axis). (**B**) We aligned sRNA-seq reads of 31-32
1269 bases in length to the RFAM database using MMSeqs2 (88). The stacked bar graph shows
1270 the percentage of reads identified as 5S, 5.8S, 18S, 28S, or tRNA, as indicated in the color-
1271 coded legend. Green, reads identified as derived from *H. vulgare*; blue, reads identified as
1272 derived from *B. hordei* DH14; grey, reads originating from neither *H. vulgare* nor *B. hordei*;
1273 purple, reads identified as *B. hordei* tRNA-derived. Apoplastic extracellular vesicles (EV+),
1274 apoplastic extracellular vesicles of non-infected control plants (EV-), and the three EV-
1275 replicates are shown. Total reads assigned to each sample are provided below the graph;
1276 circles visually indicate the total number of reads for comparison. (**C**) We aligned sRNA-seq
1277 reads of 31-32 bases to the *H. vulgare* 28S rDNA (3,853 bases). The graphs display the
1278 number of reads identified (y-axis) mapping to each position of the *H. vulgare* 28S rDNA (x-
1279 axis). Apoplastic extracellular vesicles (EV+), apoplastic extracellular vesicles of non-infected
1280 control plants (EV-), and the three replicates for EV-. *Hvu*-rRF0003 fragments were detected
1281 in EV+ and EV- samples, in addition to *Hvu*-rRF0004 (EV+) and *Hvu*-rRF0005 (EV-).
1282 *Hvu*-rRF0003 and *Hvu*-rRF0005 were otherwise detected only in replicate 3.
1283
1284 **Supplementary Figure 11. GO enrichment of putative endogenous milRNA targets.** We
1285 determined all putative targets of the sets of *B. hordei* and *H. vulgare* milRNAs via
1286 psRNAtarget (31). We used ShinyGO v0.75 (85) to calculate enriched gene ontology (GO)
1287 terms in all milRNA target sets and summarized redundant GO terms with EMBL-EBI
1288 QuickGO (https://www.ebi.ac.uk/QuickGO/) on GO version 2022-04-26 and REVIGO (86). (**A**)
1289 GO enrichment terms found in putative endogenous targets of *B. hordei* milRNAs. (**B**) GO
1290 enrichment terms found in putative endogenous targets of *H. vulgare* milRNAs. The GO
1291 terms and identifiers are indicated next to the bubble plots. Bubble size indicates fold
1292 enrichment of the term in the respective subset, fill color indicates -Log10 of the FDR-
1293 adjusted enrichment *P* value. The milRNA subsets are indicated below the bubble plots (see
1294 Figure 4 for all subsets). The icons on top of the plot were created with bioRender.com; the
1295 blue mycelium indicates *B. hordei* and the green plant barley.
1296
1297 **Supplementary Figure 12. PhasiRNAs are abundant in the *B. hordei* locus *BLGH_03674***
1298 **encoding a pseudogenized Sgk2 kinase.** PhasiRNA-rich loci indicative of phasing in the
1299 genome of *B. hordei* were detected using ShortStack pipeline v3.8.5-1 (29), the PHASIS
1300 pipeline (33), and unitas v1.7.0 (34). The figure shows an example of a phased locus in
1301 *B. hordei*, containing the gene *BLGH_03674*, which is the partial open reading frame of a
1302 gene encoding a Sgk2 kinase. From top to bottom, the position on the scaffold, scaffold
1303 name and window, gene and transposable element annotations, and sample names are
1304 indicated. Read coverage is indicated left of each mapping profile. Red lines indicate reads
1305 mapping in sense orientation of the displayed sequence window; blue lines show reads

1306 mapping in antisense orientation. The putative trans-activating RNA (tasiRNA) is indicated
1307 with an asterisk. The figure was generated after manual inspection with Integrative Genome
1308 Viewer (IGV; (87)).
1309
1310
1311

1312 Supplementary Data

1313
1314 **Supplementary File 1.** FASTA file containing all tRNA and rRNA fragments identified in this
1315 study.
1316 **Supplementary File 2.** GFF3 file with all *H. vulgare* milRNA loci identified in this study.
1317 **Supplementary File 3.** FASTA file with all *H. vulgare* milRNAs identified in this study.
1318 **Supplementary File 4.** GFF3 file with all *B. hordei* milRNA loci identified in this study.
1319 **Supplementary File 5.** FASTA file with all *B. hordei* milRNAs identified in this study.
1320
1321 **Supplementary Table 1.** General summary of sRNA sequencing samples, and sample
1322 description.
1323 **Supplementary Table 2.** Read length distribution counts of the trimmed reads across all
1324 samples.
1325 **Supplementary Table 3.** Distribution of read lengths mapped to the reference genome of *H.*
1326 *vulgare* (IBSCv2; (27)).
1327 **Supplementary Table 4.** Distribution of read lengths mapped to the reference genome of *B.*
1328 *hordei* (28).
1329 **Supplementary Table 5.** Reads from the samples were aligned by BLAST to the *H. vulgare*
1330 28S rDNA; mappings were counted in 10-base windows.
1331 **Supplementary Table 6.** Reads from the samples were aligned by BLAST to the *B. hordei* 28S
1332 rDNA; mappings were counted in 10-base windows.
1333 **Supplementary Table 7.** Secondary structure and minimum free energy (MFE) predictions of
1334 *H. vulgare* and *B. hordei* tRNA and RNA fragments
1335 **Supplementary Table 8.** Accession numbers of publicly available small RNA-seq datasets
1336 from barley, wheat, and Arabidopsis under biotic or abiotic stress.
1337 **Supplementary Table 9.** Summary of unique milRNAs detected in *B. hordei* and *H. vulgare*
1338 by ShortStack, across all samples.
1339 **Supplementary Table 10.** Counts of sRNA-seq reads mapping to the milRNA loci in *H.*
1340 *vulgare* identified by ShortStack.
1341 **Supplementary Table 11.** Counts of sRNA-seq reads mapping to the milRNA loci in *B. hordei*
1342 identified by ShortStack.
1343 **Supplementary Table 12.** GO enrichment of gene sets predicted to be targeted by *H.*
1344 *vulgare* milRNAs.
1345 **Supplementary Table 13.** GO enrichment of gene sets predicted to be targeted by *B. hordei*
1346 milRNAs.
1347 **Supplementary Table 14.** Loci and their annotation in the genome of *B. hordei* in which
1348 phasiRNAs were detected.

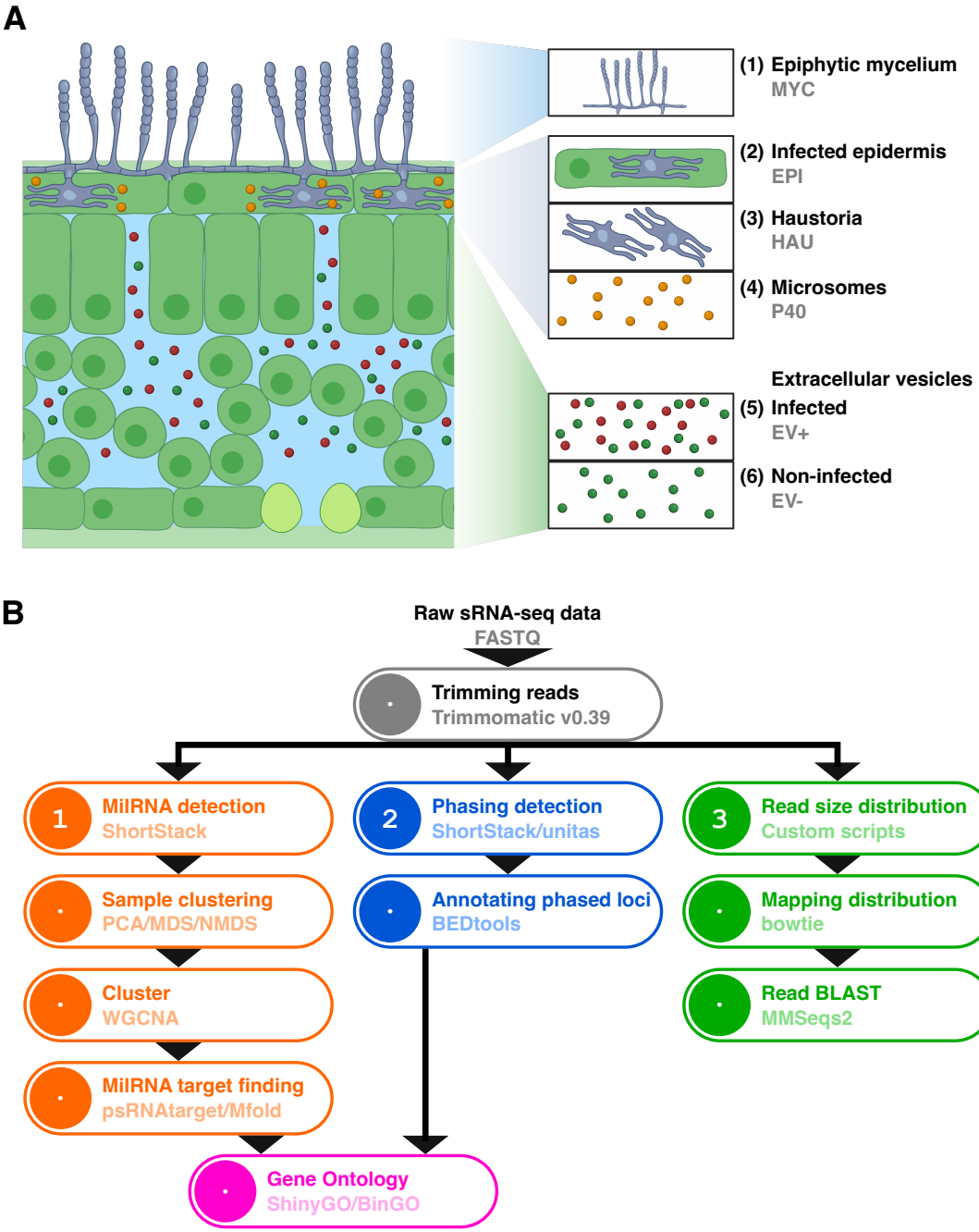

Figure 1. Isolation of total RNAs from six distinct sample types. (**A**) We isolated total RNA from the following biological materials of *B. hordei*-infected barley leaves at four days after inoculation: (1) Epiphytic fungal mycelium (MYC), (2) infected epidermis without mycelium (EPI), (3) fungal haustoria (HAU), (4) microsomes of the epidermis depleted of haustoria (P40). In addition, we isolated total RNA from (5) apoplastic extracellular vesicles of infected plants (EV+) at three days after inoculation, and (6) apoplastic extracellular vesicles from non-infected control plants (EV-). The figure was created using bioRender.com. (**B**) Bioinformatic pipeline for sRNA-seq data analysis. We analysed the sRNA-seq reads in three ways: (1) by read size and read mapping distribution to the respective genomes, followed by read BLAST against the RFAM database for particular fractions of the read data; (2) by ShortStack analysis to detect putative miIRNAs in both organisms, followed by principal component analysis for sample clustering, miIRNA expression analysis, miIRNA target prediction, and functional description of these targets by GO assignment; (3) by detection of loci enriched with predicted phasiRNAs.

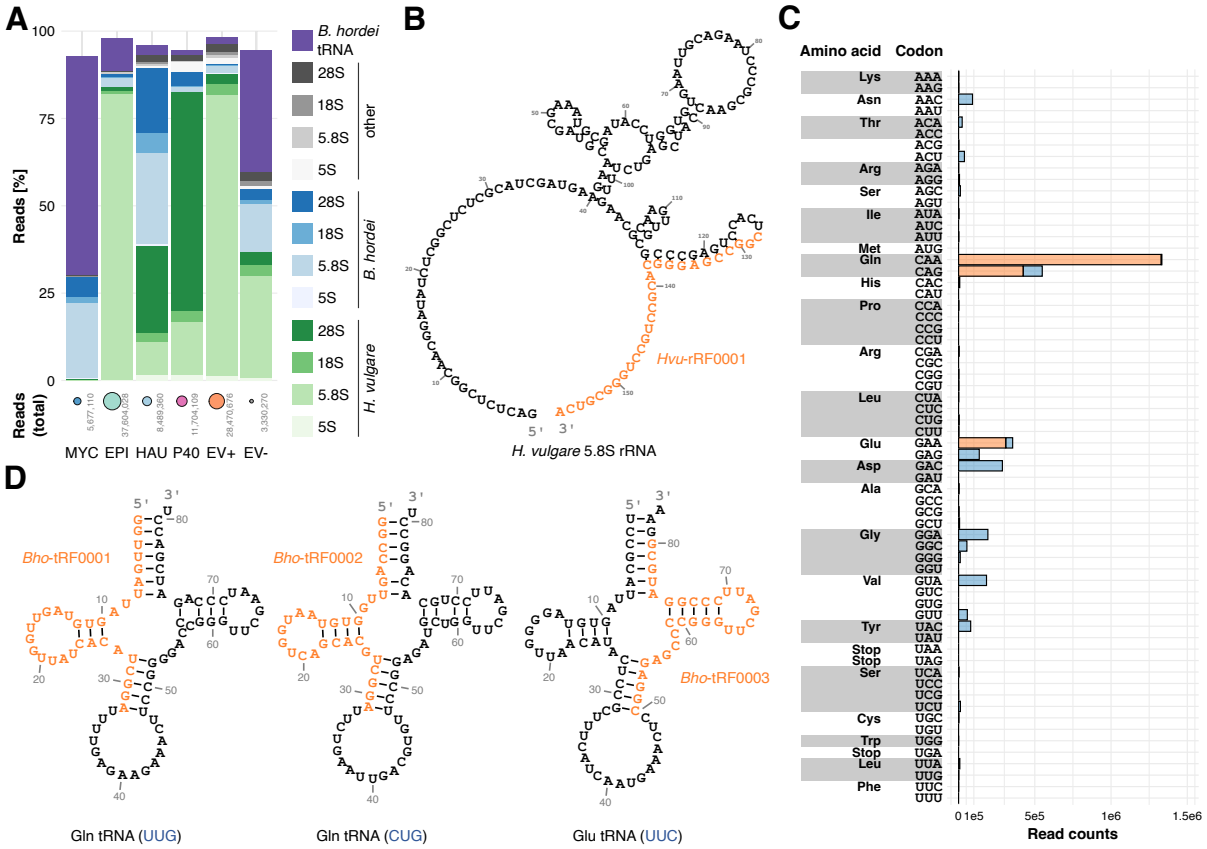

Figure 2. Specific barley 5.8S rRNA- and *B. hordei* tRNA-derived sRNAs are enriched in the 31-33 base reads. We aligned sRNA-seq reads of 31-33 bases in length to the RFAM database using MMSeqs2 (Steinegger and Söding 2017). (**A**) The stacked bar graph shows the percentage of reads identified as 5S, 5.8S, 18S (small subunit, SSU), 28S (large subunit, LSU), or tRNA, as indicated in the color-coded legend. Green, reads identified as derived from *H. vulgare*; blue, reads identified as derived from *B. hordei* DH14; grey, reads not assigned to either *H. vulgare* or *B. hordei*; purple, reads identified as *B. hordei* tRNA-derived. Epiphytic fungal mycelium (MYC), infected epidermis without mycelium (EPI), fungal haustoria (HAU), microsomes of the epidermis without haustoria (P40), apoplastic extracellular vesicles (EV+), and apoplastic extracellular vesicles of non-infected control plants (EV-). The total number of reads assigned to each sample is given below the bar graph (visualized by circle size). (**B**) Predicted secondary structure of the barley 5.8S rRNA (RFAM accession CAJW010993076.1:c203-48; RNA central accession URS0000C3A4AE_112509), calculated by R2DT in RNA central (https://rnacentral.org) and visualized with Forna (Kerpedjiev *et al.* 2015). The RNA sequence in orange indicates the over-represented 3' end in the reads from the EPI and EV+ samples. (**C**) Histogram showing the number of reads (Read counts, x-axis) accounting for the *B. hordei* tRNA-derived reads in the sample MYC. The coding amino acid and respective mRNA codons are indicated on the left. The orange portion of the histogram bars indicates the fraction of reads coming from the three most abundant tRNA fragments. (**D**) The three most abundant tRNAs represented in the MYC sample are shown; left, Gln tRNA with UUG anticodon; middle, Gln tRNA with CUG anticodon; right, Glu tRNA with UUC anticodon. The orange-labelled sequences indicate the abundant tRNA fragments.

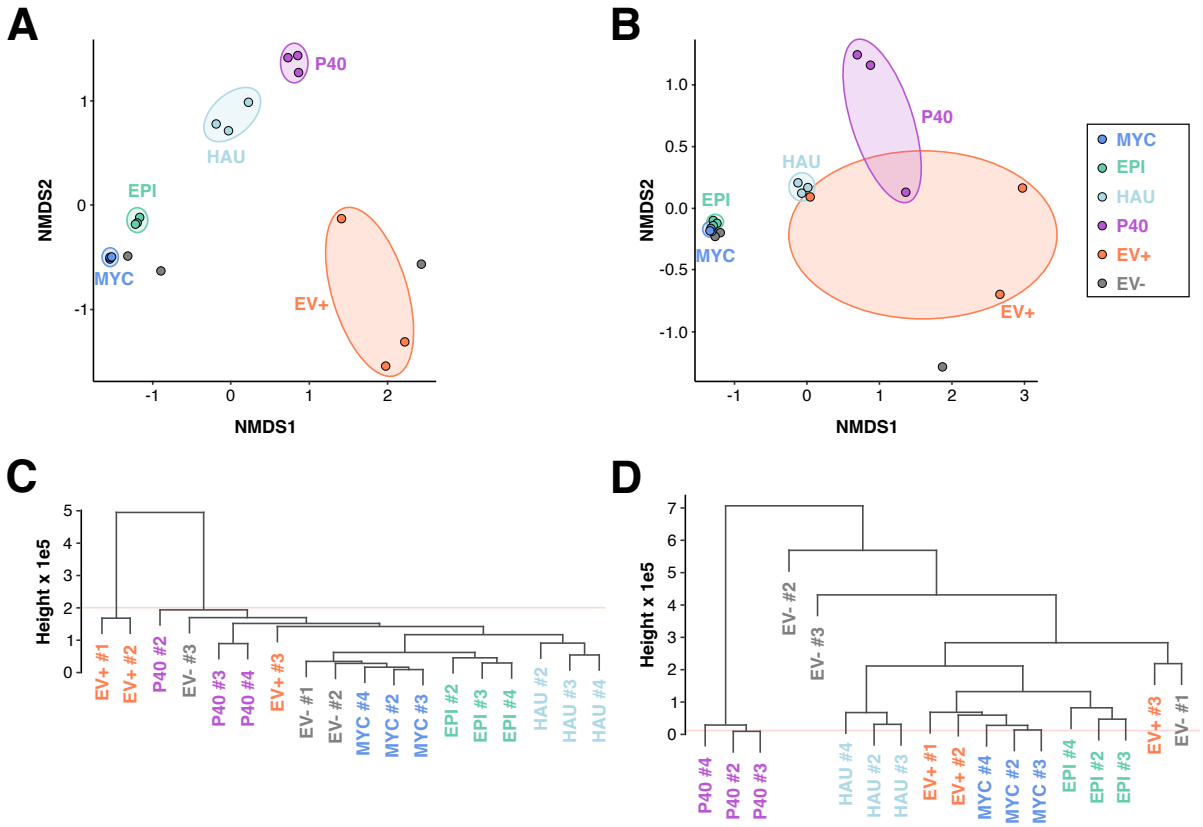

Figure 3. The milRNA content of microsomal samples differs from mycelial, epidermal, and haustorial samples. (**A**) and (**B** We used non-metric multi-dimensional scaling (NMDS), which collapses multidimensional information into two dimensions to visualize sample similarity. Each data point represents the collapsed milRNA expression data from *H. vulgare* (**A**) and *B. hordei* (**B**). Blue, epiphytic fungal mycelium (MYC); green, infected epidermis without mycelium (EPI); light blue, fungal haustoria (HAU); purple, microsomes of the epidermis without haustoria (P40); orange, apoplastic extracellular vesicles (EV+); grey, apoplastic extracellular vesicles of non-infected control plants (EV-). (**C**) and (**D**) milRNA sample distances based on a Pearson correlation matrix from the milRNA expression data. The pair-wise Pearson correlations were used to calculate a Euclidean distance tree with all samples for *H. vulgare* (**C**) and *B. hordei* (**D**).

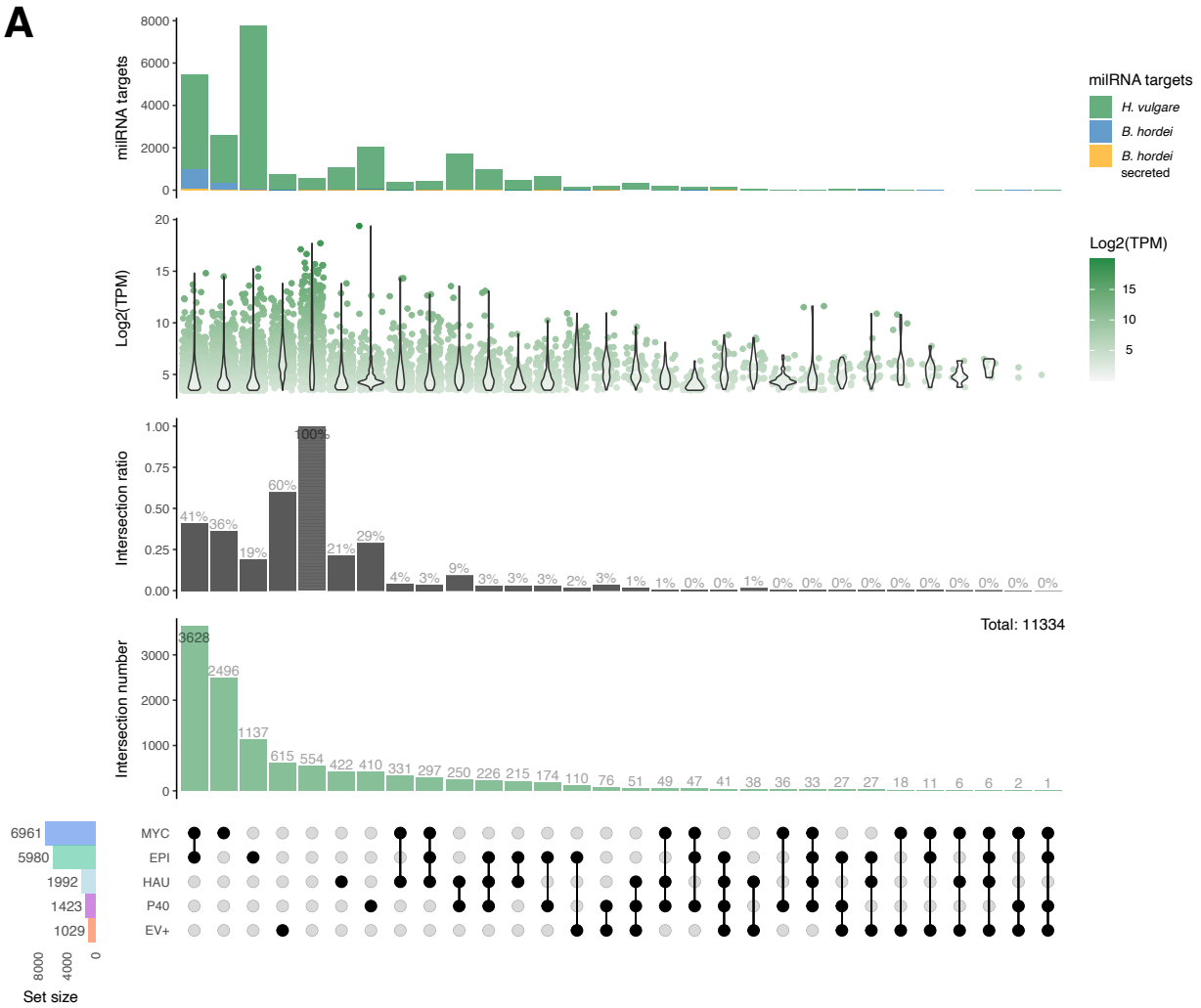
A
milRNA targets
Log2(TPM)
Intersection ratio
Intersection number
Total: 11334
MYC
EPI
HAU
P40
EV+
Set size
milRNA targets
H. vulgare
B. hordei
B. hordei secreted
Log2(TPM)

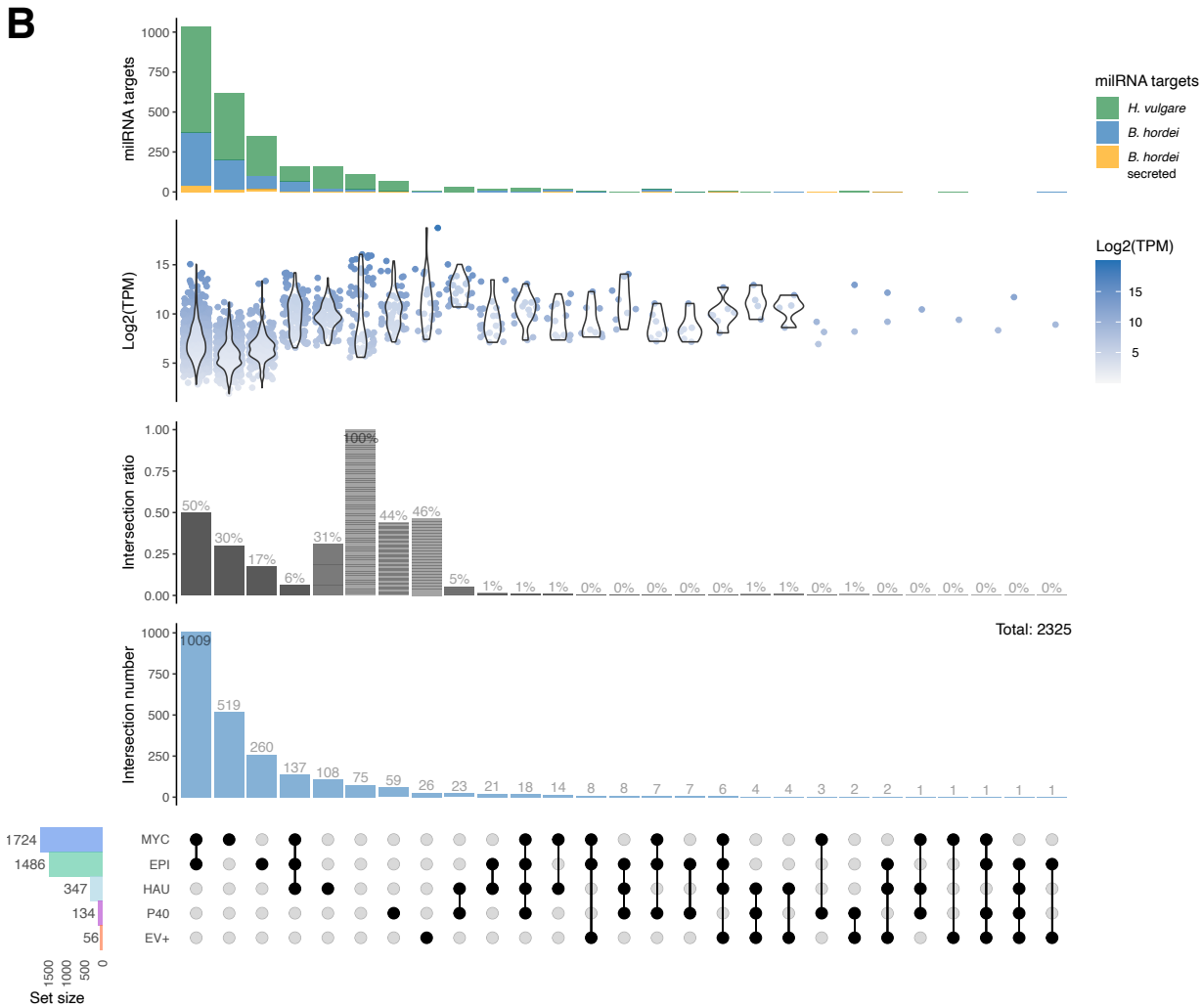
B
milRNA targets
Log2(TPM)
Intersection ratio
Intersection number
Total: 2325
MYC
EPI
HAU
P40
EV+
Set size
milRNA targets
H. vulgare
B. hordei
B. hordei secreted
Log2(TPM)

Figure 4. Large sets of milRNAs exhibit site-specific distribution. We calculated site-specific abundance in MYC, EPI, HAU, P40, and EV+ samples for (**A**) *H. vulgare* and (**B**) *B. hordei* using WGCNA and assigned milRNAs to samples exhibiting >2.5-fold enrichment over the average. The bottom panels indicate the set sizes of milRNAs in the respective samples (bar graph, left); blue, epiphytic fungal mycelium (MYC); green, infected epidermis without mycelium (EPI); light blue, fungal haustoria (HAU); purple, microsomes of the epidermis without haustoria (P40); orange, apoplastic extracellular vesicles (EV+). The dots indicate the samples contributing to the respective interaction sets. The second panels from the bottom are bar graphs of the intersection numbers, which are the numbers of milRNAs in the exclusive intersections. The third panels from the bottom show the normalized abundance of the milRNAs in the respective interaction sets as violin plot; the maximum TPM value across samples was used for each data point. The top panels are stacked bar charts of the sum of predicted milRNA target genes in *B. hordei* (blue) and *H. vulgare* (green); *B. hordei* genes encoding a secreted protein are shown in orange.

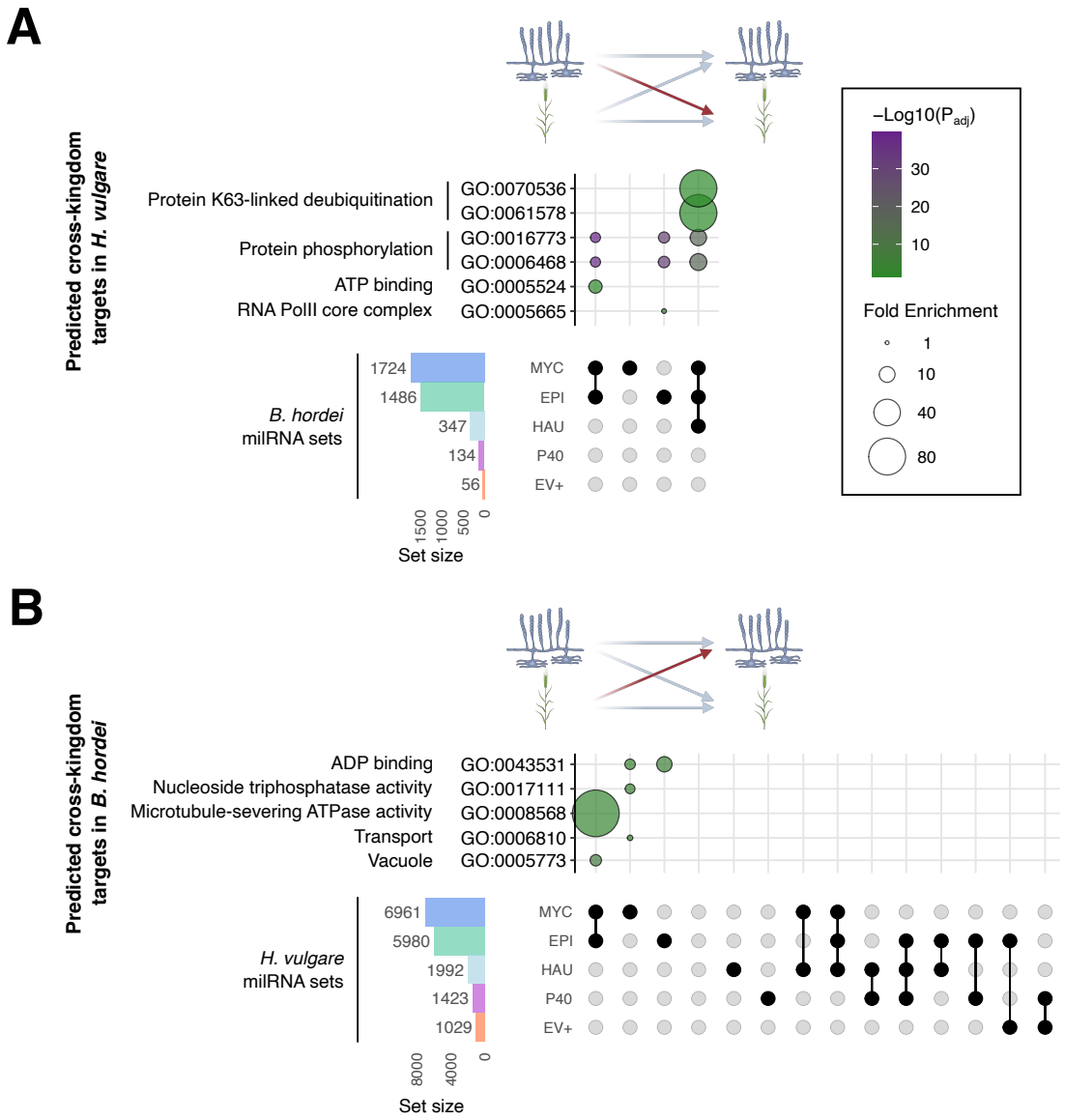

Figure 5. GO enrichment analysis of putative cross-kingdom milRNA targets. We determined all putative targets of the sets of *B. hordei* and *H. vulgare* milRNAs via psRNAtarget (Dai and Zhao 2011). We used ShinyGO v0.75 (Ge *et al.* 2020) to calculate enriched gene ontology (GO) terms in all milRNA target sets and summarized redundant GO terms with EMBL-EBI QuickGO (https://www.ebi.ac.uk/QuickGO/) on GO version 2022-04-26 and REVIGO (Supek *et al.* 2011). (**A**) GO enrichment terms found in putative cross-kingdom targets of *B. hordei* milRNAs in *H. vulgare*. (**B**) GO enrichment terms found in putative cross-kingdom targets of *H. vulgare* milRNAs in *B. hordei*. The GO terms and identifiers are indicated next to the bubble plots. Bubble size indicates fold enrichment of the term in the respective subset, fill color indicates -Log10 of the FDR-adjusted enrichment *P* value. The milRNA subsets are indicated below the bubble plots (see Figure 4 for all subsets). The icons on top of the plot were created with bioRender.com; the blue mycelium indicates *B. hordei* and the green plant barley.

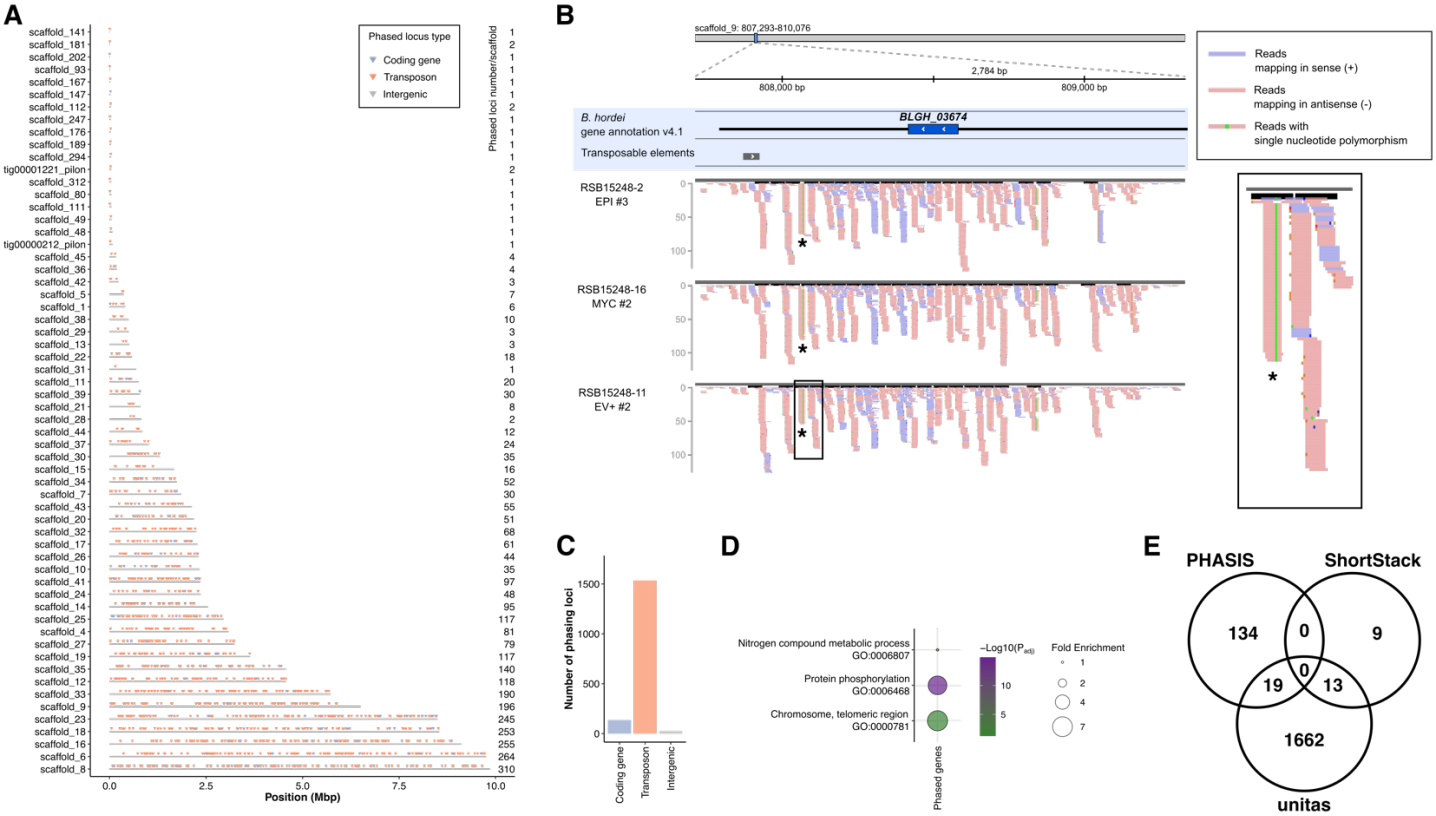

Figure 6. Transposable elements and Sgk2 kinases are subject to phasing in *B. hordei*. We identified phasiRNA-rich loci indicative of phasing in the genome of *B. hordei* with ShortStack pipeline v3.8.5-1 (Johnson *et al.* 2016), the PHASIS pipeline (Kakrana *et al.* 2017), and unitas v1.7.0 (Gebert *et al.* 2017). (**A**) Global distribution of predicted phasing loci in the genome of *B. hordei* DH14 (Frantzeskakis *et al.* 2018). The x-axis shows the genome position in mega base pairs (Mbp) and the scaffolds are indicated on the y-axis. Triangles denote loci in which phasiRNAs were found with unitas. Blue triangles, phasing loci coinciding with annotated coding genes; orange triangles, phasing loci coinciding with transposable elements; grey triangles, intergenic phasing loci. (**B**) Example of one phased locus in *B. hordei*, containing the gene *BLGH_03674*, the partial open reading frame of a gene encoding a Sgk2 kinase. A subset of representative samples from sites where phasing in this locus was detected is shown (EPI, MYC, and EV+), the full set of samples is displayed in Supplementary Figure 12. From top to bottom, the position on the scaffold, scaffold name and window, gene and transposable element annotations, and sample names are indicated. Red lines indicate reads mapping in sense orientation of the displayed sequence window; blue lines show reads mapping in antisense orientation. A zoom-in is shown on the right. The putative trans-activating RNA (tasiRNA) is indicated with an asterisk. The figure was generated after inspection with Integrative Genome Viewer (IGV; (Robinson *et al.* 2017)). (**C**) Bar graph summarizing the number of phasing loci types. The x-axis indicates the locus type, i.e., coding gene, transposon, or intergenic; the y-axis shows the number of loci. (**D**) GO enrichment of phased coding genes was calculated with ShinyGO v0.75 (Ge *et al.* 2020); terms were summarized to non-redundant GO terms with EMBL-EBI QuickGO (https://www.ebi.ac.uk/QuickGO/) on GO version 2022-04-26 and REVIGO (Supek *et al.* 2011). The bubble size indicates fold enrichment of the term in the respective subset, fill color indicates -Log10 of the FDR-adjusted enrichment *P* value. (**E**) A Venn diagram summarizing the overlap of discovered phasing loci with the three methods.